Mass and momentum conservation of the Least-Squares Spectral Collocation Method for the Navier-Stokes equations

Thorsten Kattelans[1]   Wilhelm Heinrichs[2]

Abstract

From the literature it is known that the LSSEM for the stationary Stokes equations performs poorly with respect to mass conservation but compensates this lack by a superior conservation of momentum. Furthermore, it is known that the LSSCM leads to superior conservation of mass and momentum for the stationary Stokes equations. In the present paper we consider mass and momentum conservation of the LSSCM for time-dependent Stokes and Navier-Stokes equations. We observe that the LSSCM leads to improved conservation of mass (and momentum) for these problems. Furthermore, the LSSCM leads to the well-known time-dependent profiles for the velocity and the pressure profiles. To obtain these results we use only a few elements, each with high polynomial degree, avoid normal equations for solving the overdetermined linear systems of equations and introduce the Clenshaw-Curtis quadrature rule for imposing the average pressure to be zero. Furthermore, we combined the transformation of Gordon and Hall (transfinite mapping) with the least-squares spectral collocation scheme to discretize the internal flow problems.

Keywords: incompressible Navier-Stokes equations, internal flow, spectral collocation, least-squares, transfinite mapping, Clenshaw-Curtis quadrature, QR, LSSCM

1   Introduction

Spectral methods (see, e.g., Canuto et al. [2], Gottlieb and Orszag [9, 26] or Deville et.al. [5]) employ global polynomials for the numerical solution of differential equations.

---

[1]thorsten.kattelans@uni-due.de

[2]wilhelm.heinrichs@uni-due.de

University of Duisburg-Essen, Engineering Mathematics, Universitaetsstr. 3, D-45117 Essen, Germany

Hence they give very accurate approximations for smooth solutions with relatively few degrees of freedom. For sufficiently smooth data exponential convergence can be achieved.

If one deals with problems with non-smooth solutions the usual (global) spectral approach yields very poor approximation results. To avoid these difficulties the original domain can be decomposed into several sub domains and least-squares techniques can be applied, see e.g. [10, 12–15], [22–24], [28–30] and [31–35]. Least-squares techniques for such problems offer theoretical and numerical advantages over the classical Galerkin type methods which must fulfill the well-posedness (or stability) criterion, the so called LBB condition. The advantage of least-squares techniques is that they lead to positive definite algebraic systems which circumvent the LBB stability condition, see, e.g. [1, 17–19, 21]. One very special least-squares technique is the least-squares spectral element method, see, e.g. [6, 16, 32–34]. These least-squares spectral element methods (see, e.g. [20]) for the Stokes problem were first introduced by Gerritsma and Proot in [31, 32]. Spectral least-squares for the Navier-Stokes equations were first presented by Pontaza and Reddy in [28–30], followed by Gerritsma and Proot in [34]. Heinrichs investigated least-squares spectral collocation schemes in [12–15] that lead to symmetric and positive definite algebraic systems which circumvent the LBB stability condition. Furthermore, Heinrichs and Kattelans presented in [15, 23] least-squares spectral collocation schemes where they improved the conditions numbers of the algebraic systems, considered different types of decompositions of the domain and different interface conditions between the elements for the Stokes and Navier-Stokes equations. In [24] they have shown that the Least-Squares Spectral Collocation Method (LSSCM) leads to improved conservation of mass and momentum for an internal flow problem for the stationary Stokes equations.

Here, we consider internal flow problems to investigate mass and momentum conservation of the LSSCM for the time-dependent Stokes equations and for the Navier-Stokes equations. A typical example of such a flow problem is a small channel of width h in which a cylinder with diameter d moves along the centerline of the channel, see e.g. [4, 24, 35].

In [4] it has been shown for the stationary Stokes equations that the Least-Squares Finite Element Method (LSFEM) leads to an unsatisfactory velocity profile along the smallest cross-section between the channel wall and the cylinder. Using this calculated velocity profile to calculate the mass flow through the cross-section it has been observed that the calculated mass flow is significantly lower than the mass inflow into the channel.

2

The important questions is:

> Why are least-squares methods more susceptible to loss of mass conservation than, e.g., Galerkin-type methods?

The main reason why least-squares methods are more susceptible to loss of mass conservation than Galerkin methods is that they are based on minimization of a functional which includes the continuity equation. In contrast to Galerkin-type methods the mass conservation, i.e. $\nabla \cdot \mathbf{u} = 0$ is a constraint. Because of this, the continuity equations play a different role in the least-squares formulation from the role it plays in Galerkin. Thus, it is clear why least-squares methods are more susceptible to loss of mass conservation than "direct methods".

One way overcoming the problem of the LSFEM is using the so called restricted LSFEM, see [4], which is based on the least-squares functional with the extension of mass conservation $\nabla \cdot \mathbf{u} = 0$.

Proot and Gerritsma have shown in [33, 35] that the Least-Squares Spectral Element Method (LSSEM) leads to good results for such flow problems, since the LSSEM compensate the loss of mass conservation by a superior conservation of the momentum equations for the stationary Stokes equations.

Kattelans and Heinrichs have shown for the stationary Stokes equations in [24] that the LSSCM leads to improved conservation of mass and momentum for internal flow problems. The main reasons for their improved results were that the domain was decomposed into only a few elements, the transfinite mapping of Gordon and Hall was used for discretization, the Clenshaw-Curtis quadrature rule was used for the additional pressure integral condition and the resulting overdetermined algebraic systems were solved by QR decomposition.

In this paper we continue the study in [24] for the time-dependent Stokes equations and for the Navier-Stokes equations and we will show that the LSSCM leads to improved mass <u>and</u> momentum conservation for this equations, too.

Furthermore, our approach has the following advantages:

- equal order interpolation polynomials can be employed

- it is possible to vary the polynomial order from element to element

- improved stability properties for small perturbation parameters in singular perturbation problems, [10] and Stokes or Navier-Stokes equations [12–15, 23]

- improved conservation of mass and momentum for the stationary Stokes equations, [24]

- good performance in combination with domain decomposition techniques

- direct and efficient iterative solvers for positive definite systems can be used

- implementation is straightforward.

The paper is organized in the following way. In Section 2, the internal flow problem is described. Section 3 introduces the first-order formulation of the Stokes equations and the Navier-Stokes equations. The LSSCM and the discretization are presented in Section 4. The numerical results of our simulations are discussed in Section 5, where we present our results for the time-dependent Stokes equations in Section 5.1 and for the Navier-Stokes equations in Section 5.2. The Conclusion is presented in Section 6.

2 The problem set-up

In order to investigate the mass and momentum conservation of the LSSCM we use the same test case as in [4, 24, 33, 35]. The flow problem is defined by a cylinder of diameter d which moves at a speed of one along the centerline of a channel of width $h = 1.5$, see Fig. 1.
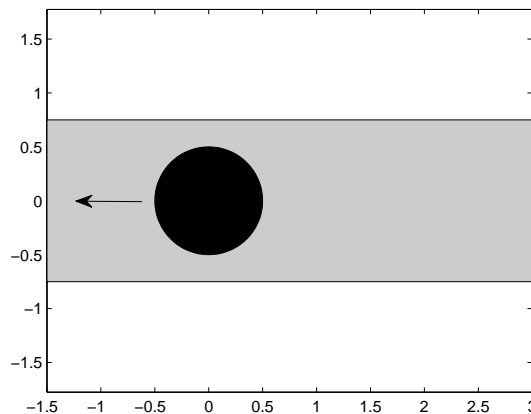

Figure 1: *The problem set-up on* $\Omega_{0.5}$

The domain of the channel is defined as a rectangle and the center of the cylinder is located at the origin, i.e. we solve the partial differential equations on the domain

$$\Omega_r := \Omega_c \backslash K_r,$$

where $\Omega_c := [-1.5, 3] \times [-0.75, 0.75]$ and $K_r := \{(x, y) \in \mathbb{R}^2 : x^2 + y^2 < r^2\}$. The boundary conditions of the velocity are given by

$$\mathbf{u}_{|\partial\Omega} := \begin{cases} [1, 0]^T & \text{on} \quad \partial\Omega_c \\ \\ [0, 0]^T & \text{on} \quad \partial K_r \end{cases}.$$

3 The Stokes and Navier-Stokes equations

In order to apply least-squares the Stokes and Navier-Stokes problems are transformed into an equivalent first-order system of partial differential equations. This is accomplished by introducing the vorticity $\omega = \nabla \times \mathbf{u}$ as an auxiliary variable. By using the identity

$$\nabla \times \nabla \times \mathbf{u} = -\Delta \mathbf{u} + \nabla(\nabla \cdot \mathbf{u})$$

and the incompressibility constraint $\nabla \cdot \mathbf{u} = 0$ we obtain

$$\frac{\partial \mathbf{u}}{\partial t} + \nu \nabla \times \omega + \nabla p = \mathbf{f} \quad \text{in } \Omega_r , \, t \in [0, t_{end}] \tag{1}$$

$$\nabla \cdot \mathbf{u} = 0 \quad \text{in } \Omega_r , \, t \in [0, t_{end}] \tag{2}$$

$$\omega - \nabla \times \mathbf{u} = 0 \quad \text{in } \Omega_r , \, t \in [0, t_{end}] \tag{3}$$

for the Stokes equations and for the Navier-Stokes equations we obtain

$$\frac{\partial \mathbf{u}}{\partial t} + \mathbf{u} \cdot \nabla \mathbf{u} + \nu \nabla \times \omega + \nabla p = \mathbf{f} \quad \text{in } \Omega_r , \, t \in [0, t_{end}] \tag{4}$$

$$\nabla \cdot \mathbf{u} = 0 \quad \text{in } \Omega_r , \, t \in [0, t_{end}] \tag{5}$$

$$\omega - \nabla \times \mathbf{u} = 0 \quad \text{in } \Omega_r , \, t \in [0, t_{end}] \tag{6}$$

where $\mathbf{u}^T = [u_1, u_2]$ denotes the velocity vector, p the pressure, $\mathbf{f}^T = [f_1, f_2]$ the forcing term and ν the kinematic viscosity. Here it is assumed that the density equals unity. Since the pressure is through (1)-(3) or (4)-(6) only determined up to a constant for the Stokes or Navier-Stokes equations we have to introduce an additional condition for the pressure. One procedure is to impose the pressure at an arbitrary point of the given domain. Another

way of dealing with the pressure constant is imposing the average pressure to be zero; i.e.,

$$\int_{\Omega_r} p \, d\mathbf{x} = 0. \tag{7}$$

3.1 The Stokes equations

For the Stokes equations we use for time integration a second-order BDF scheme (see, e.g., [15]): If Δt denotes the step size in t and the index $n+1$ indicates that the functions are evaluated at the time step $t_{n+1} = (n+1)\Delta t$, $n = 0, 1, 2, \ldots$, the approximation of $(\frac{\partial \mathbf{u}}{\partial t})^{n+1}$ can be written as

$$\frac{\frac{3}{2}\mathbf{u}^{n+1} - 2\mathbf{u}^n + \frac{1}{2}\mathbf{u}^{n-1}}{\Delta t}. \tag{8}$$

Now the complete system at time step t_{n+1} can explicitly be written as:

$$\begin{pmatrix} \dfrac{3}{2\Delta t} & 0 & \nu\dfrac{\partial}{\partial x_2} & \dfrac{\partial}{\partial x_1} \\[2ex] 0 & \dfrac{3}{2\Delta t} & -\nu\dfrac{\partial}{\partial x_1} & \dfrac{\partial}{\partial x_2} \\[2ex] \dfrac{\partial}{\partial x_2} & -\dfrac{\partial}{\partial x_1} & 1 & 0 \\[2ex] \dfrac{\partial}{\partial x_1} & \dfrac{\partial}{\partial x_2} & 0 & 0 \end{pmatrix} \begin{pmatrix} u_1^{n+1} \\[2ex] u_2^{n+1} \\[2ex] \omega^{n+1} \\[2ex] p^{n+1} \end{pmatrix} = \begin{pmatrix} g_1^{n+1} \\[2ex] g_2^{n+1} \\[2ex] 0 \\[2ex] 0 \end{pmatrix} \quad \text{in } \Omega_r, \tag{9}$$

where

$$\mathbf{g}^{n+1} = \mathbf{f}^{n+1} + \frac{2}{\Delta t}\mathbf{u}^n - \frac{1}{2\Delta t}\mathbf{u}^{n-1}.$$

3.2 The Navier-Stokes equations

For the Navier-Stokes equations we use an implicit and explicit scheme.

3.2.1 Implicit scheme

As proposed in [15, 34], we apply a θ-integration scheme in time combined with the Picard linearization to the momentum equations of the unsteady

6

Navier-Stokes equations. The subscript "0" corresponds to the results obtained at a previous integration time step. Now the momentum equations read as follows:

$$\frac{\mathbf{u} - \mathbf{u}_0}{\Delta t} + \theta(\mathbf{u}_0 \cdot \nabla \mathbf{u} + \nabla p + \nu \nabla \times \omega - \mathbf{f})$$
$$= (\theta - 1)(\mathbf{u}_0 \cdot \nabla \mathbf{u}_0 + \nabla p_0 + \nu \nabla \times \omega_0 - \mathbf{f}_0) \tag{10}$$

By taking $\theta = 1$, the time integration is carried out by the backward Euler method, which is only first-order accurate in time. The second-order time integration of Crank-Nicolson can be obtained by setting $\theta = 1/2$. Since the Crank-Nicolson scheme has no damping, one often takes $\theta = 1/2 + \mathcal{O}(\Delta t)$. The temporal accuracy remains second-order, and adding the small factor Δt effectively damps the small waves in spectral element simulations. Hence, in order to obtain time-accurate solutions, one should use $\theta = 1/2 + \mathcal{O}(\Delta t)$. The θ-scheme is unconditionally stable for $1/2 \leq \theta \leq 1$. Now the complete system for each time step can explicitly be written as:

$$Az = r \tag{11}$$

where

$$A = \begin{pmatrix} \frac{1}{\Delta t} + \theta u_{1,0}\frac{\partial}{\partial x_1} + \theta u_{2,0}\frac{\partial}{\partial x_2} & 0 & \theta\nu\frac{\partial}{\partial x_2} & \theta\frac{\partial}{\partial x_1} \\ 0 & \frac{1}{\Delta t} + \theta u_{1,0}\frac{\partial}{\partial x_1} + \theta u_{2,0}\frac{\partial}{\partial x_2} & -\theta\nu\frac{\partial}{\partial x_1} & \theta\frac{\partial}{\partial x_2} \\ \frac{\partial}{\partial x_2} & -\frac{\partial}{\partial x_1} & 1 & 0 \\ \frac{\partial}{\partial x_1} & \frac{\partial}{\partial x_2} & 0 & 0 \end{pmatrix},$$

$z = (u_1, u_2, \omega, p)^T$ and

$$r = \begin{pmatrix} f_1 + \frac{u_{1,0}}{\Delta t} + (\theta - 1)\left[u_{1,0}\frac{\partial u_{1,0}}{\partial x_1} + u_{2,0}\frac{\partial u_{1,0}}{\partial x_2} + \nu\frac{\partial \omega_0}{\partial x_2} + \frac{\partial p_0}{\partial x_1}\right] \\ f_2 + \frac{u_{2,0}}{\Delta t} + (\theta - 1)\left[u_{1,0}\frac{\partial u_{2,0}}{\partial x_1} + u_{2,0}\frac{\partial u_{2,0}}{\partial x_2} + \nu\frac{\partial \omega_0}{\partial x_1} + \frac{\partial p_0}{\partial x_2}\right] \\ 0 \\ 0 \end{pmatrix}.$$

3.2.2 Explicit scheme

For time integration we also employ a semi-implicit scheme where the second order backward differentiation scheme (8) for the viscous term is combined with a second order Adams-Bashforth scheme for the convective term. Hence the momentum equations (4) at time step $t_{n+1} = (n+1)\Delta t$, $n = 0, 1, 2, \ldots$ can be written as:

$$\frac{3}{2\Delta t}\mathbf{u}^{n+1} + \nu \nabla \times \omega^{n+1} + \nabla p^{n+1} = \mathbf{g}^{n+1} \tag{12}$$

where

$$\mathbf{g}^{n+1} = \mathbf{f}^{n+1} - 2\mathbf{C}^n + \mathbf{C}^{n-1} + \frac{2}{\Delta t}\mathbf{u}^n - \frac{1}{2\Delta t}\mathbf{u}^{n-1} \tag{13}$$

with the convective term $\mathbf{C} = (\mathbf{u} \cdot \nabla)\mathbf{u}$.

Now the complete system at time step t_{n+1} can explicitly be written as:

$$
\begin{pmatrix}
\dfrac{3}{2\Delta t} & 0 & \nu\dfrac{\partial}{\partial x_2} & \dfrac{\partial}{\partial x_1} \\[2mm]
0 & \dfrac{3}{2\Delta t} & -\nu\dfrac{\partial}{\partial x_1} & \dfrac{\partial}{\partial x_2} \\[2mm]
\dfrac{\partial}{\partial x_2} & -\dfrac{\partial}{\partial x_1} & 1 & 0 \\[2mm]
\dfrac{\partial}{\partial x_1} & \dfrac{\partial}{\partial x_2} & 0 & 0
\end{pmatrix}
\begin{pmatrix}
u_1^{n+1} \\[2mm]
u_2^{n+1} \\[2mm]
\omega^{n+1} \\[2mm]
p^{n+1}
\end{pmatrix}
=
\begin{pmatrix}
g_1^{n+1} \\[2mm]
g_2^{n+1} \\[2mm]
0 \\[2mm]
0
\end{pmatrix}
\quad \text{in } \Omega_r. \tag{14}
$$

The big advantage of the explicit scheme is that the matrix has to be set up once. During time integration we only have to compute matrix-vector multiplications which are very fast. By numerical experiments we found out that for a well balanced system it is recommended to scale the momentum equations by Δt, as in [12, 15, 23]. Then for the least-squares scheme the incompressibility condition is well balanced against the momentum equations. In particular, we observed that without scaling the scheme becomes divergent for increasing Reynolds numbers since the diagonal entries $3/2\Delta t$ become large for decreasing step size, see, e.g. Figure 6 in [15].

4   The Least-Squares Spectral Collocation Method

For the spectral approximation we introduce the polynomial subspace

$$\mathbb{P}_N = \{\text{Polynomials of degree} \leq N \text{ in both variables } x_1, x_2\}.$$

Now all unknown functions are approximated by polynomials of the same degree N, i.e., u_1, u_2, ω, p are approximated by interpolating polynomials u_1^N, u_2^N, ω^N, $p^N \in \mathbb{P}_N$. Furthermore, we have to introduce the standard Chebyshev Gauss-Lobatto (CGL) collocation nodes which are explicitly given by

$$(\xi_i, \eta_j) = \left(-\cos\left(\frac{i\pi}{N}\right), -\cos\left(\frac{j\pi}{N}\right) \right), \quad i,j = 0, \ldots, N. \tag{15}$$

In the following we write the spectral derivatives. First one has to introduce the transformation matrices from physical space to coefficient space. Since we employ a Chebyshev expansion we obtain the following matrix:

$$T = (t_{i,j}) = \left(\cos\left(j\frac{(N-i)\pi}{N} \right) \right), \quad i,j = 0, \ldots, N.$$

Further, we need the differentiation matrix in the Chebyshev coefficient space which is explicitly given by $\hat{D} = (\hat{d}_{i,j}) \in \mathbb{R}^{N+1,N+1}$ with

$$\hat{d}_{i,j} = \begin{cases} \dfrac{2j}{c_i} & , \quad j = i+1, i+3, \ldots, N \\ 0 & , \quad \text{else} \end{cases}$$

and

$$c_i = \begin{cases} 2 & , \quad i = 0 \\ 1 & , \quad \text{else.} \end{cases}$$

Now we are able to write explicitly the spectral derivative matrix D for the first derivative which is given by

$$D = T\hat{D}T^{-1} \in \mathbb{R}^{N+1,N+1}. \tag{16}$$

The spectral operator can be efficiently evaluated by Fast Fourier Transformations (FFTs) in $\mathcal{O}(N \log N)$ arithmetic operations. We further introduce the identity matrix $I \in \mathbb{R}^{N+1,N+1}$. By tensor product representation $A \otimes B = (Ab_{i,j})_{i,j}$ we are now able to write the spectral derivatives:

$$\frac{\partial}{\partial x} \cong D_1 := D \otimes I \quad , \quad \frac{\partial}{\partial y} \cong D_2 := I \otimes D. \tag{17}$$

Next we have to realize the discrete formulation of equation (7). This is performed by the Clenshaw-Curtis quadrature rule (see, e.g. [27]):

$$\int_{\Omega_s} p\, d\mathbf{x} \cong \sum_{i=0}^{N} \sum_{j=0}^{N} \omega_i \omega_j p(\xi_i, \eta_j)$$

where $\Omega_s := [-1,1]^2$ denotes the standard domain, (ξ_i, η_j) the Chebyshev Gauss-Lobatto nodes on Ω_s and

$$\omega_i := \begin{cases} \dfrac{1}{N^2 - 1} & , \quad i \in \{0, N\} \\ \dfrac{4}{N} \displaystyle\sum_{j=0}^{\frac{N}{2}} \dfrac{1}{\bar{c}_j} \dfrac{\cos\left(\frac{2\pi ij}{N}\right)}{1 - 4j^2} & , \quad 1 \leq i \leq N - 1 \end{cases}$$

with

$$\bar{c}_j := \begin{cases} 2 & , \quad j \in \{0, N/2\} \\ 1 & , \quad 1 \leq j \leq N/2 - 1 \end{cases}$$

the integration weights.

We use the Clenshaw-Curtis quadrature rule since this is the appropriate quadrature rule for the Chebyshev Gauss-Lobatto nodes.

One could also use Gauss Legendre or Gauss Lobatto-Legendre nodes. In the numerical results there is no big difference, see, e.g. [37]. The advantage of the Chebyshev nodes is the fact that they are explicitly given and fast Fourier transforms (FFTs) are available.

Furthermore, we have to decompose the domain Ω_r into quadrilaterals (some with curved boundaries). Since we consider a smooth problem and for spectral least-squares methods it is better to use only a few elements for such problems, each with high polynomial degree (see, e.g. [24]), we here use only 12 elements, i.e.

$$\Omega_r = \bigcup_{i=1}^{12} \widehat{\Omega}_i,$$

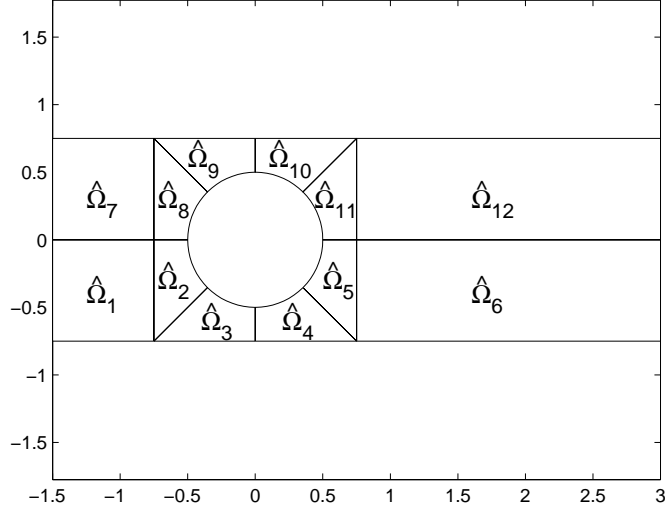where $\widehat{\Omega}_i$, $i = 1, \ldots, 12$ are defined as in Figure 2.

Figure 2: *Decomposition of $\Omega_{0.5}$ into 12 elements*

For the other domains Ω_r we use the similar decomposition.

In order to apply the least-squares spectral collocation scheme, we have to define a transformed problem on the square. Instead of introducing polar coordinates we prefer the transfinite mapping of Gordon and Hall, see, e.g. [2, 7, 8, 11]. The advantage of the transfinite mapping of Gordon and Hall is that it is a very simple transformation where no singularities (as by using polar coordinates) occur, see, e.g. [11].

To construct the mapping Ψ_i of the square $\Omega_s = [-1, 1]^2$ with boundaries Γ_ν into one of the quadrilaterals $\widehat{\Omega}_i$ with (curved) boundaries $\widehat{\Gamma}_\nu^i$ we use the mappings

$$\pi_\nu^i : \Gamma_\nu \longrightarrow \widehat{\Gamma}_\nu^i \quad , \quad i = 1, \dots, 12 \quad , \quad \nu = 1, \dots, 4.$$

As an example, in the following we write the functions π_ν^2, $\nu = 1, \dots, 4$, for

element $\widehat{\Omega}_2$:

$$\pi_1^2(\xi) = \begin{pmatrix} \dfrac{1}{2}\left[(-0.5+0.75)\xi - 0.75 - 0.5\right] \\ 0 \end{pmatrix},$$

$$\pi_2^2(\eta) = \begin{pmatrix} -0.75 \\ \dfrac{1}{2}\left[(0+0.75)\eta - 0.75 + 0\right] \end{pmatrix},$$

$$\pi_3^2(\xi) = \begin{pmatrix} \dfrac{1}{2}\left[\left(-\dfrac{1}{2\sqrt{2}} + 0.75\right)\xi - \dfrac{1}{2\sqrt{2}} - 0.75\right] \\ \dfrac{1}{2}\left[\left(-\dfrac{1}{2\sqrt{2}} + 0.75\right)\xi - \dfrac{1}{2\sqrt{2}} - 0.75\right] \end{pmatrix},$$

$$\pi_4^2(\eta) = \begin{pmatrix} -\sqrt{0.5^2 - \left\{\dfrac{1}{2}\left[\left(0+\dfrac{1}{2\sqrt{2}}\right)\eta - \dfrac{1}{2\sqrt{2}} + 0\right]\right\}^2} \\ \dfrac{1}{2}\left[\left(0+\dfrac{1}{2\sqrt{2}}\right)\eta - \dfrac{1}{2\sqrt{2}} + 0\right] \end{pmatrix},$$

where $(\xi, \eta) \in \Omega_s$ are the standard CGL nodes.

Following Gordon and Hall, the mapping $\Psi_2 : \Omega_s \longrightarrow \widehat{\Omega}_2$ can be written explicitly in terms of the π_ν^2 as:

$$\begin{aligned} \Psi_2(\xi, \eta) &= \frac{1-\eta}{2}\pi_3^2(\xi) + \frac{1+\eta}{2}\pi_1^2(\xi) \\ &\quad + \frac{1-\xi}{2}\left[\pi_2^2(\eta) - \frac{1+\eta}{2}\pi_2^2(1) - \frac{1-\eta}{2}\pi_2^2(-1)\right] \\ &\quad + \frac{1+\xi}{2}\left[\pi_4^2(\eta) - \frac{1+\eta}{2}\pi_4^2(1) - \frac{1-\eta}{2}\pi_4^2(-1)\right]. \end{aligned} \quad (18)$$

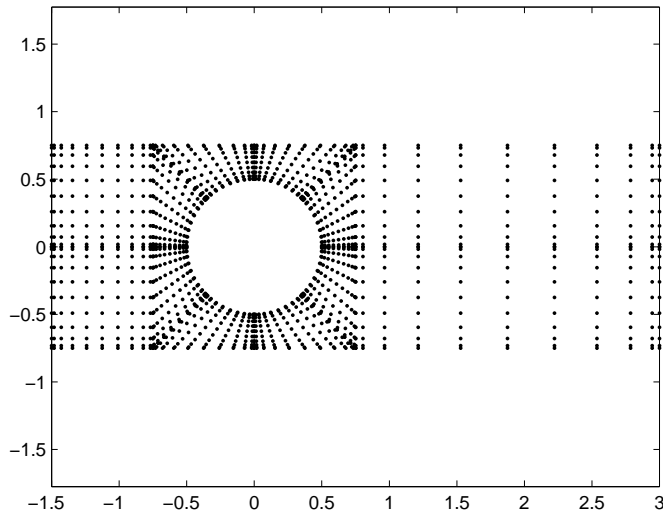The whole discretization of $\Omega_{0.5}$ is shown in Figure 3.

Figure 3: *Discretization of $\Omega_{0.5}$, where polynomial degree $N = 10$ is used on each element*

Since we are interested in the solution of an first-order partial differential equation we have to transform the first-order partial derivatives from the coordinates $(\xi, \eta) \in \Omega_s$ into the coordinates $(x, y) \in \widehat{\Omega}_i$, $i = 1, \ldots, 12$. The coordinates of $\widehat{\Omega}_i$ are given as functions $x = x(\xi, \eta)$ and $y = y(\xi, \eta)$. Hence, the transformation reads as follows:

$$\left(\begin{array}{c} u_x \\ u_y \end{array} \right) = \frac{1}{x_\xi y_\eta - x_\eta y_\xi} \left(\begin{array}{cc} y_\eta & -y_\xi \\ -x_\eta & x_\xi \end{array} \right) \left(\begin{array}{c} u_\xi \\ u_\eta \end{array} \right).$$

At the interfaces between the elements we enforce pointwise C^0 interface conditions of all functions, i.e. continuity of the velocity, continuity of the vorticity and continuity of the pressure. One could also require (as Heinrichs and Kattelans in [14, 15, 23]) continuity of both the functions and normal derivatives of u_1, u_2, continuity for p and no explicit interface condition for ω. In the numerical results there are no nameable differences concerning these two different types of interface conditions, see [23]. The reason, we here use C^0 interface conditions is, the resulting linear systems of equations have lower condition numbers and the dimension of the matrices are smaller.

The corresponding discrete system of differential equations together with the discrete boundary, the discrete interface conditions and the discrete version of

13

(7) are written into a matrix A and compiled into an overdetermined system $Az = r$ where the matrix A is given by

$$A = \begin{pmatrix} A_1 & & & \\ & \ddots & & \\ & & A_{12} & \\ & M_I & & \\ & B & & \\ & M_p & & \end{pmatrix}. \tag{19}$$

Here A_i (dense matrix), $i = 1, \ldots, 12$ denotes the discrete version of the matrix in (9) and (14), respectively, on the corresponding element $\widehat{\Omega}_i$. The matrix M_I represents the discrete interface conditions, B the given discrete boundary conditions for the velocity components u_1 and u_2 and M_p the additional discrete pressure condition in (7). In [15] we have shown, that these types of linear systems of equations are really overdetermined and it is better to use QR decomposition for solving these systems instead of forming the normal equations. The reason is, the normal equations square the condition numbers of the algebraic systems and because of this the round-off errors have a stronger influence. Hence, all overdetermined linear systems of equations in this paper are solved by QR decomposition. Another approach can be found in [16].

5   Numerical simulations

For the numerical simulations we first define a smooth model problem to verify the spectral accuracy of the proposed scheme. The velocity and the pressure for the model problem are defined by

$$u_1(x, y, t) \quad := \quad \cos(\gamma t) \sin\left(\frac{\pi x}{2}\right) \cos\left(\frac{\pi y}{2}\right) \tag{20}$$

$$u_2(x, y, t) \quad := \quad -\cos(\gamma t) \cos\left(\frac{\pi x}{2}\right) \sin\left(\frac{\pi y}{2}\right) \tag{21}$$

$$p(x, y, t) \quad := \quad \frac{1}{4}\cos^2(\gamma t)(\sin(\pi x) + \sin(\pi y)) + 10(x + y)\cos(\gamma t), \tag{22}$$

where $(x, y, t) \in \Omega_r \times [0, \infty)$. By choosing $\gamma = 0$ or $\gamma \neq 0$ we can change between a steady or unsteady problem.

5.1   Unsteady Stokes equations

First, we consider the unsteady Stokes equations, where we consider the smooth model problem followed by the simulations of the internal flow prob-

lem. All simulations of the unsteady Stokes equations are performed on $\Omega_{0.5}$.

5.1.1 Smooth model problem

Now, we consider the unsteady Stokes equations on the channel $\Omega_{0.5}$. Since we consider the unsteady Stokes equations we set $\gamma = 5$ in (20) – (22). Verifying the stability of the proposed scheme, we first consider the smooth model problem with small time step size and a long time interval. In Figures 4 and 5 we show the approximation errors of the velocity component u_2 and of the pressure for this long time integration. For velocity component u_1 we obtain similar results and so we do not show them here.
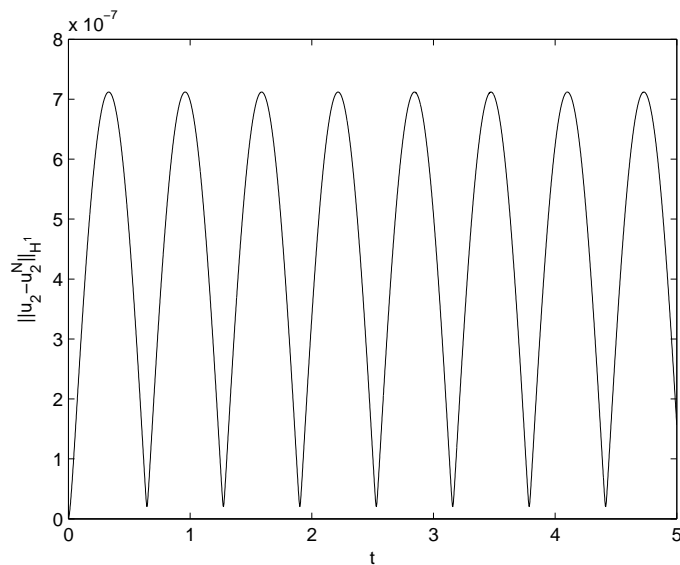
Figure 4: *The unsteady model problem for the Stokes equations on $\Omega_{0.5}$: Temporal evolution of $||u_2 - u_2^N||_{H^1}$ for $N = 16$, $\Delta t = \frac{1}{1000}$ and $\nu = 1$*
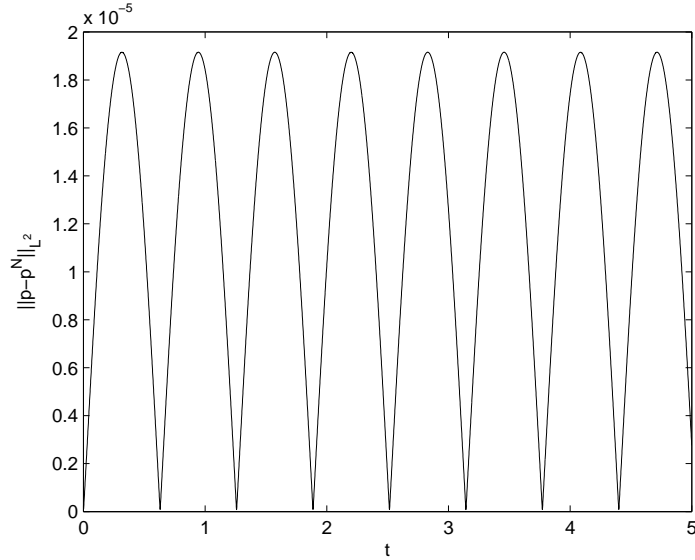
Figure 5: *The unsteady model problem for the Stokes equations on $\Omega_{0.5}$: Temporal evolution of $||p - p^N||_{L^2}$ for $N = 16$, $\Delta t = \frac{1}{1000}$ and $\nu = 1$*

From Figures 4 and 5 we observe no enlargement of the oscillating errors in time, expressing stability of the numerical solution.

In the Tables 1 – 3 we show the approximation errors for the unsteady Stokes equations and we see the good performance of the here presented scheme for time-dependent problems. We set

$$
\begin{aligned}
E_{u_1} &:= \max\{||u_1 - u_1^N||_{H^1} : t \in [0, 1]\}, \\
E_{u_2} &:= \max\{||u_2 - u_2^N||_{H^1} : t \in [0, 1]\}, \\
E_p &:= \max\{||p - p^N||_{L^2} : t \in [0, 1]\},
\end{aligned}
$$

since Figures 4 and 5 show that the maximum errors are obtained in $[0, 1]$.

Δt	E_{u_1}	ratio	E_{u_2}	ratio	E_p	ratio
$\frac{1}{10}$	$1.040 \cdot 10^{-2}$	—	$6.955 \cdot 10^{-3}$	—	$1.880 \cdot 10^{-1}$	—
$\frac{1}{20}$	$2.642 \cdot 10^{-3}$	3.936	$1.768 \cdot 10^{-3}$	3.934	$4.767 \cdot 10^{-2}$	3.944
$\frac{1}{40}$	$6.630 \cdot 10^{-4}$	3.985	$4.436 \cdot 10^{-4}$	3.986	$1.195 \cdot 10^{-2}$	3.989
$\frac{1}{80}$	$1.659 \cdot 10^{-4}$	3.996	$1.110 \cdot 10^{-4}$	3.996	$2.992 \cdot 10^{-3}$	3.994
$\frac{1}{160}$	$4.148 \cdot 10^{-5}$	4.000	$2.775 \cdot 10^{-5}$	4.000	$7.482 \cdot 10^{-4}$	3.999
$\frac{1}{320}$	$1.037 \cdot 10^{-5}$	4.000	$6.938 \cdot 10^{-6}$	4.000	$1.871 \cdot 10^{-4}$	3.999

Table 1: *The unsteady model problem for the Stokes equations on $\Omega_{0.5}$: E_{u_1}, E_{u_2} and E_p for $N = 18$, $\nu = 1$ and different Δt*

Δt	E_{u_1}	ratio	E_{u_2}	ratio	E_p	ratio
$\frac{1}{10}$	$3.197 \cdot 10^{-1}$	—	$1.829 \cdot 10^{-1}$	—	$1.726 \cdot 10^{-1}$	—
$\frac{1}{20}$	$8.543 \cdot 10^{-2}$	3.742	$4.875 \cdot 10^{-2}$	3.752	$4.378 \cdot 10^{-2}$	3.942
$\frac{1}{40}$	$2.164 \cdot 10^{-2}$	3.948	$1.239 \cdot 10^{-2}$	3.935	$1.097 \cdot 10^{-2}$	3.991
$\frac{1}{80}$	$5.429 \cdot 10^{-3}$	3.986	$3.108 \cdot 10^{-3}$	3.986	$2.750 \cdot 10^{-3}$	3.989
$\frac{1}{160}$	$1.359 \cdot 10^{-3}$	3.995	$7.780 \cdot 10^{-4}$	3.995	$6.877 \cdot 10^{-4}$	3.999

Table 2: *The unsteady model problem for the Stokes equations on $\Omega_{0.5}$: E_{u_1}, E_{u_2} and E_p for $N = 18$, $\nu = \frac{1}{100}$ and different Δt*

Δt	E_{u_1}	ratio	E_{u_2}	ratio	E_p	ratio
$\frac{1}{10}$	$6.105 \cdot 10^{-1}$	—	$3.444 \cdot 10^{-1}$	—	$1.719 \cdot 10^{-1}$	—
$\frac{1}{20}$	$1.625 \cdot 10^{-1}$	3.757	$9.127 \cdot 10^{-2}$	3.773	$4.363 \cdot 10^{-2}$	3.940
$\frac{1}{40}$	$4.130 \cdot 10^{-2}$	3.935	$2.306 \cdot 10^{-2}$	3.958	$1.087 \cdot 10^{-2}$	4.014

Table 3: *The unsteady model problem for the Stokes equations on $\Omega_{0.5}$: E_{u_1}, E_{u_2} and E_p for $N = 18$, $\nu = \frac{1}{400}$ and different Δt*

Tables 1 – 3 present the good performance of the scheme. Furthermore, we observe that the ratios converges to 4. Since we use a second order scheme in time, the ratio of, e.g. E_{u1} with time step size Δt and E_{u1} with time step size $\Delta t/2$ must approximate $2^\lambda = 4$, where $\lambda = 2$ denotes the order of the time integration scheme.

5.1.2 Channel flow

Now, we consider the time-dependent Stokes equations to simulate the internal flow problem. Neither Chang and Nelson in [4] nor Gerritsma and Proot in [33, 35] nor Heinrichs and Kattelans in [24] studied the time-dependent Stokes flow. We declare the internal flow as an stationary problem and assume that the steady state is reached if

$$\varepsilon := \frac{\max |\phi^{n+1} - \phi^n|}{\Delta t \cdot \max |\phi^{n+1}|} \leq 10^{-8}, \tag{23}$$

where $\phi := (u_1, u_2)^T$, is fulfilled. Here, $|\cdot|$ is the vector with the absolute value of its components.

To simulate the internal flow problem for the time-dependent Stokes equations we set here $N = 18$ and $\Delta t = \frac{1}{10}$. Furthermore, we consider the unsteady Stokes equations for different viscosities to show the performance

17

of the scheme for different test-cases. It is clear that the different viscosities are not physically motivated but numerically.

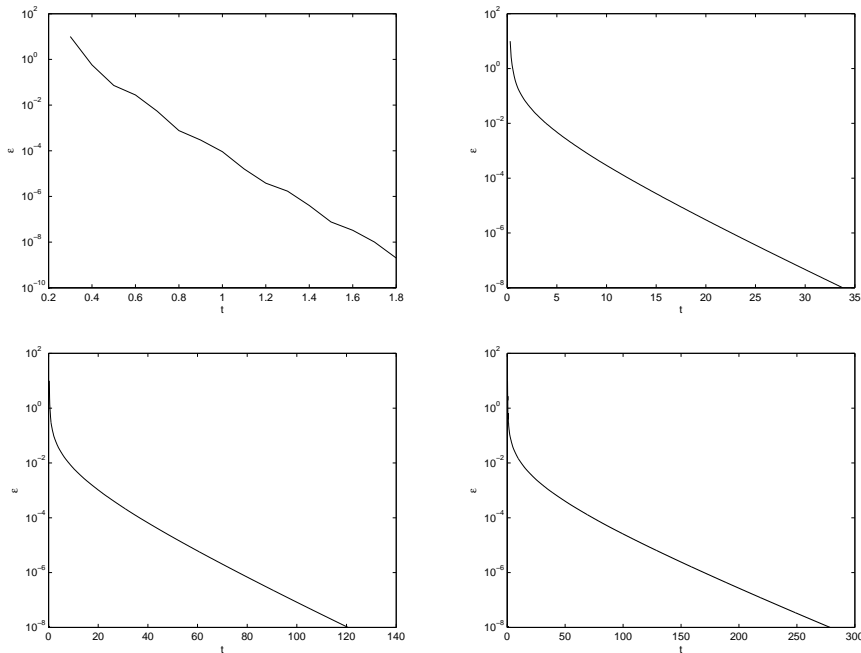In Figure 6 we show the temporal evolution of ε for different ν.

Figure 6: *Unsteady Stokes flow past the cylinder on $\Omega_{0.5}$: Temporal evolution of ε for $\nu = 1$ (upper left), $\nu = \frac{1}{100}$ (upper right), $\nu = \frac{1}{400}$ (lower left) and $\nu = \frac{1}{1000}$ (lower right)*

We see the well-known performance of the scheme that (23) is fulfilled later for decreasing viscosity, i.e the increasing number of iterations for decreasing viscosity. Furthermore, we observe the strictly monotonic decreasing of ε during time integration. This again represents the stability of the proposed numerical method.

Next, we study the loss of mass in the cross-section γ_2, as in [24], which is given by

$$\mathcal{M} := \frac{1}{2} \int_{\gamma_1} u_1 \, ds - \int_{\gamma_2} u_1 \, ds, \tag{24}$$

where

$$\gamma_1 := \{(-1.5, y) : -0.75 \leq y \leq 0.75\} \tag{25}$$
$$\gamma_2 := \{(0, y) : 0.5 \leq y \leq 0.75\} \tag{26}$$

18

The line integrals in (24) are approximated by the Clenshaw-Curtis quadrature rule, again. To avoid the influence of the quadrature rule to the approximations of $\mathcal{M}$ in (24) and thus the conclusions drawn from the date, we use refined grids for the approximation of the integrals. Our simulations have shown that the numerical integration on refined grids has no effect on the conclusions, since the error between the first two computed values is less than 10^{-10}.

The percentaged loss of mass is denoted by $\mathcal{M}\%$. The temporal evolution of $|\mathcal{M}|$ and of $\mathcal{M}\%$ are shown in Figure 7.
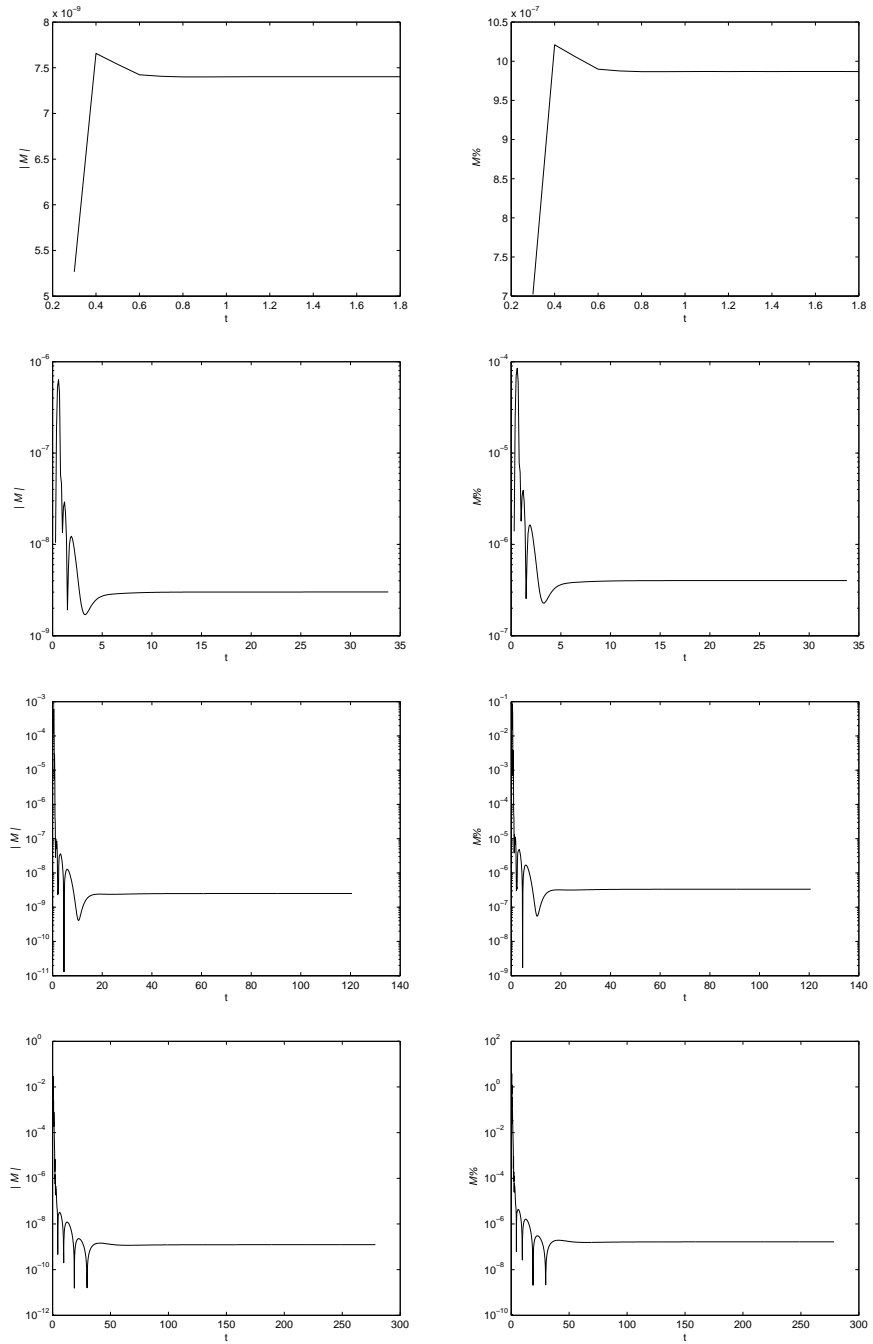
Figure 7: *Unsteady Stokes flow past the cylinder on* $\Omega_{0.5}$*: Temporal evolution of* $|\mathcal{M}|$ *(left) and* $\mathcal{M}\%$ *(right) for* $\nu = 1$ *(first row),* $\nu = \frac{1}{100}$ *(second row),* $\nu = \frac{1}{400}$ *(third row) and* $\nu = \frac{1}{1000}$ *(fourth row)*

We observe that the LSSCM leads to improved conservation of mass in the cross-section for all here considered viscosities. The oscillating of the values at the beginning of time integration is clear, since we use a second-order BDF scheme and set $\mathbf{u}^T = [0,0]$ for $t = 0$ and for $t = \Delta t$. Because of this, the LSSCM first has to overcome the problem with the wrong initial values for the time integration scheme. When this is compensated our computations show the same value during time integration. Furthermore, we observe that mass is conserved better for decreasing viscosity. To understand this performance of the proposed scheme, we first look at Figure 8. There we discuss this phenomenon in detail. In Figure 8 we show the conservation of mass and momentum in the whole domain $\Omega_{0.5}$ during time integration. For conservation of momentum we consider the left hand side of the partial differential equation in (1), i.e. we consider

$$\mathcal{L}(U^{n+1}) := \frac{\frac{3}{2}\mathbf{u}^{n+1} - 2\mathbf{u}^n + \frac{1}{2}\mathbf{u}^{n-1}}{\Delta t} + \nu\nabla \times \omega^{n+1} + \nabla p^{n+1},$$

where $U^{n+1} = (u_1^{n+1}, u_2^{n+1}, \omega^{n+1}, p^{n+1})$.

Here, we use in each time step the computed solution (on CGL nodes) and evaluate it on CG nodes to obtain the real conservation properties. Since we collocate on CGL nodes, we verify the conservation of mass and momentum on Chebyshev Gauss (CG) nodes. Using CGL nodes to verify mass and momentum conservation is not the right way, since then one only studies the least-squares errors of the scheme and not the "really" conservation properties. The CG nodes on the standard domain Ω_s are explicitly given by

$$(\xi_i^{CG}, \eta_j^{CG}) = \left(-\cos\left(\frac{(2i+1)\pi}{2N+2}\right), -\cos\left(\frac{(2j+1)\pi}{2N+2}\right)\right), \quad i, j = 0, \ldots, N. \tag{27}$$

The corresponding transformation matrix between physical and coefficient space is given by

$$T^{CG} = (t_{i,j}^{CG}) = \cos\left(j\frac{2(N-i)+1}{2N+2}\pi\right), \quad i, j = 0, \ldots, N. \tag{28}$$

Evaluating the divergence of the velocity field and the momentum equations on CG nodes we use the computed (on CGL nodes) solutions of $\mathbf{u}$, ω and p and evaluate them on CG nodes. Hence, we need the matrix for the first derivative, which is given by

$$D^{CG} = T^{CG}\hat{D}T^{-1} \in \mathbb{R}^{N+1,N+1},$$

where $\hat{D}$ and T are given as in (16). Transformations to obtain the CG nodes and the derivative matrices on the corresponding element $\widehat{\Omega}_i$, $i = 1, \ldots, 12$ of Ω_r are performed as described in Section 4, again.
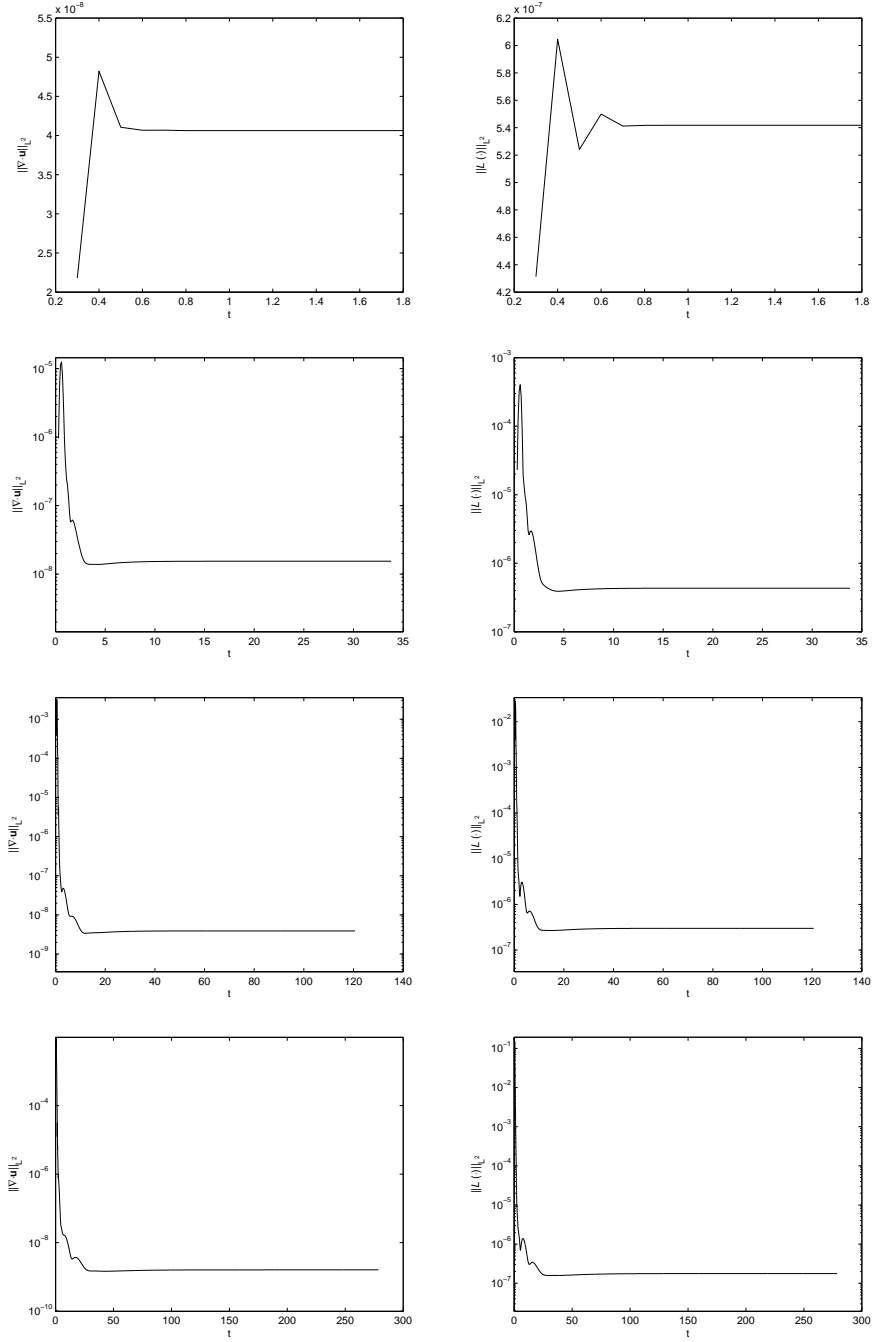
21

Figure 8: *Unsteady Stokes flow past the cylinder on $\Omega_{0.5}$: Mass and momentum conservation in the whole domain during time integation, $||\nabla\cdot\mathbf{u}||_{L^2}$ (left) and $||\mathcal{L}(U)||_{L^2}$ (right) for $\nu = 1$ (first row), $\nu = \frac{1}{100}$ (second row), $\nu = \frac{1}{400}$ (third row) and $\nu = \frac{1}{1000}$ (fourth row)*

Again, we observe the improved conservation properties of the LSSCM. In the whole domain we see an similar performance during time integration as within the cross-section, i.e. at the beginning of time integration the values oscillate slightly and after that the values are constant. The reasons are described above. Furthermore, we observe from Figure 8 that $||\nabla \cdot \mathbf{u}||_{L^2}$ decreases for decreasing viscosity. The reason of this behaviour is that for smaller viscosities the influence of the momentum equations to the whole system becomes less and because of this the continuity equation is stronger weighted in the overdetermined system. This means that the scheme leads to a "natural weighting" of the continuity equation for the time-dependent Stokes flow around the cylinder. These insights are the key to understand the analog performance of the scheme, concerning better mass conservation along the cross-section γ_2 for decreasing ν, as shown in Figure 7.

For the momentum equations we see approximately the same conservation properties of the proposed scheme for the different viscosities in Figure 8.

The numerical values of $||\nabla \cdot \mathbf{u}||_{L^2}$, $||\mathcal{L}(U)||_{L^2}$ and χ in the last time step are presented in Table 4, where

$$\chi := \max\{u_1(0, y) \,:\, 0.5 \leq y \leq 0.75\}$$

for different viscosities. Furthermore, in Table 4 we present the required number of iterations and the time t_{max} when the steady state is reached, i.e. when (23) is fulfilled. We present the numerical values of $||\nabla \cdot \mathbf{u}||_{L^2}$, $||\mathcal{L}(U)||_{L^2}$ and χ in the last time step since we have seen in Figure 8 that the temporal evolution is constant when the oscillations at the beginning are overcome.

ν	$||\nabla \cdot \mathbf{u}||_{L^2}$	$||\mathcal{L}(U)||_{L^2}$	χ	t_{max}	# iterations
1	$4.063 \cdot 10^{-8}$	$5.418 \cdot 10^{-7}$	4.2036	1.80	16
$\frac{1}{100}$	$1.543 \cdot 10^{-8}$	$4.323 \cdot 10^{-7}$	4.2036	33.80	336
$\frac{1}{400}$	$3.912 \cdot 10^{-9}$	$2.997 \cdot 10^{-7}$	4.2036	120.60	1204
$\frac{1}{1000}$	$1.602 \cdot 10^{-9}$	$1.771 \cdot 10^{-7}$	4.2036	278.60	2784

Table 4: *Unsteady Stokes flow past the cylinder on $\Omega_{0.5}$: Conservation values and maximum velocity along γ_2 in the last time step, t_{max} and number of iterations for different viscosities*

From Table 4 we observe that we reach a slightly better conservation of momentum for decreasing viscosity. But these improvements are only marginal. This performance is again caused by a "natural weighting" within the momentum equations. For smaller viscosities, the gradient of the pressure has

a stronger influence compared to $\nabla \times \omega$ in momentum equation. This disadvantage for the vorticity (defined by $\omega - \nabla \times \mathbf{u} = 0$) is compensated by the stronger influence of the continuity equation $\nabla \cdot \mathbf{u} = 0$. Because of this, mass and momentum is conserved better for decreasing ν.

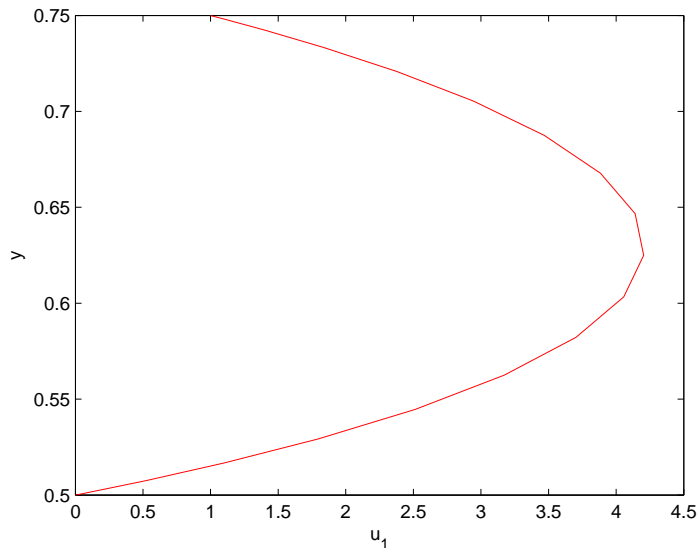In Figure 9 we show the profile of u_1 along the cross-section in the last time step t_{max}.

Figure 9: *Unsteady Stokes flow past the cylinder on $\Omega_{0.5}$: u_1 along γ_2 in the last time step*

For all considered viscosities $\nu \in \{1, \frac{1}{100}, \frac{1}{400}, \frac{1}{1000}\}$ we obtain the same plots, since the different viscosities do not influence the results for the Stokes equations. Comparing this plot with the one of the steady Stokes flow in [24], we see the good performance of the proposed scheme for time-dependent Stokes flows, again.

In Figure 10 we show the profile of u_1 and the velocity profile in the whole domain $\Omega_{0.5}$. Again, we obtain for all considered viscosities the same results, as expected.
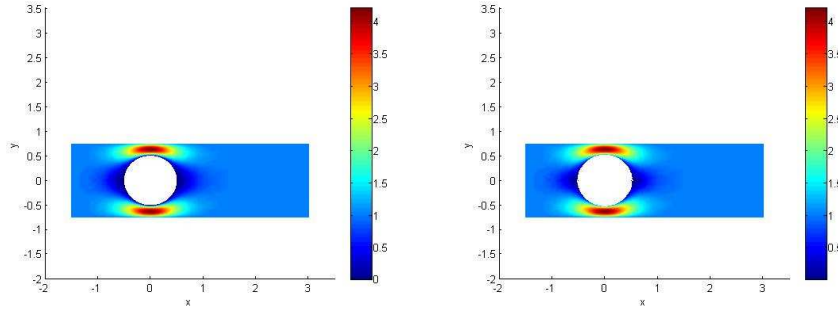
Figure 10: *Unsteady Stokes flow past the cylinder on $\Omega_{0.5}$: Profile of u_1 (left) and velocity profile $\mathbf{u}$ (right)*

Comparing the plots of Figure 10 with the one of the steady Stokes flow in [24], we see that the LSSCM is able to resolve the velocity in the whole domain for the unsteady Stokes flow very well, too.

In Figure 11 we show the pressure in the whole domain.
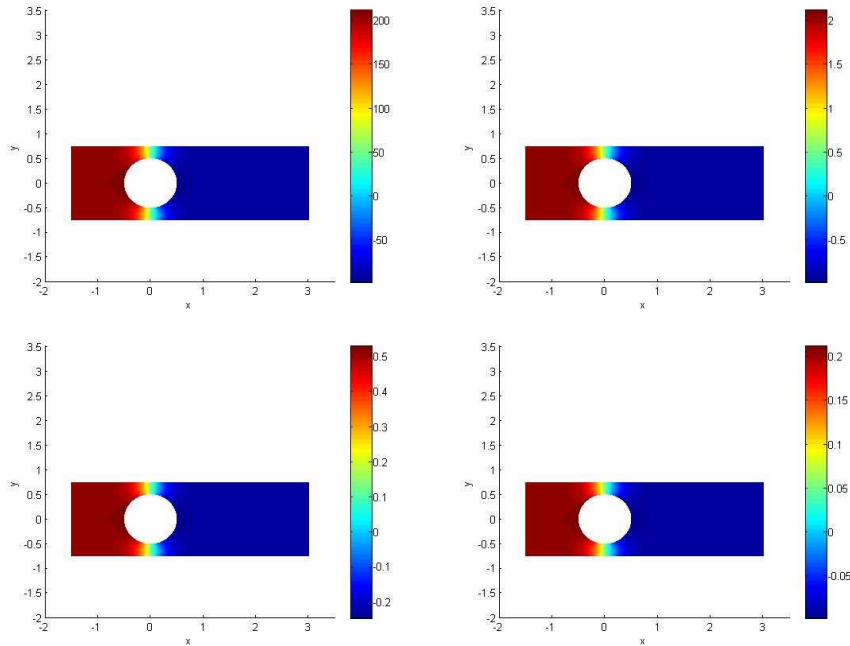
Figure 11: *Unsteady Stokes flow past the cylinder on $\Omega_{0.5}$: Pressure profile $\nu = 1$ (upper left), $\nu = \frac{1}{100}$ (upper right), $\nu = \frac{1}{400}$ (lower left) and $\nu = \frac{1}{1000}$ (lower right)*

As for the steady Stokes flows we see here the good performance for the

unsteady case, too. Because of the different viscosities it is clear that we get different maximum and minimum values for the pressure. Furthermore, we observe that for all considered viscosities we obtain analog pressure profile, as expected.

5.2 Navier-Stokes equations

Next, we consider the Navier-Stokes flow around the cylinder. To verify the proposed scheme, we first consider the smooth steady example on $\Omega_{0.5}$ (i.e. (20)–(22) with $\gamma = 0$) followed by a smooth unsteady example on $\Omega_{0.5}$ (i.e. (20)–(22) with $\gamma = 5$). Hereafter, we simulate the flow around a cylinder on $\Omega_{0.125}$ for different Reynolds numbers. The reason we consider $\Omega_{0.125}$ for the flow problem is to see the properties of the flow for different Reynolds numbers. Using the test cases with larger cylinder we can not observe the performance from the plots in the best way.

For all computations we use the explicit scheme (with Δt-scaled momentum equations), where we combine the second order BDF scheme for the viscous term with the second order Adams-Bashforth scheme for the convective term. Our simulations have shown that using the implicit scheme requires a much larger among of CPU-time. The reason is that within the implicit scheme in each time step the algebraic systems must be solved several times. Using the explicit scheme, the QR decomposition of the overdetermined algebraic systems must be solved only once. Hereafter, only matrix vector multiplications must be carry out, which are very fast. In [15] we studied the performance of explicit versus implicit scheme. The result was, that both of the schemes lead to analog results, where the implicit scheme requires a much larger amount of CPU-time.

5.2.1 Steady model problem

For the steady model problem we set $\gamma = 0$ in (20) – (22) on $\Omega_{0.5}$ to verify the spectral convergence of the proposed scheme. In Table 5 we show the numerical results.

N	$\|u_1 - u_1^N\|_{H^1}$	$\|u_2 - u_2^N\|_{H^1}$	$\|p - p^N\|_{L^2}$	$\|\nabla \cdot \mathbf{u}\|_{L^2}$
2	$3.848 \cdot 10^{-1}$	$4.425 \cdot 10^{-1}$	$1.016 \cdot 10^{0}$	$8.017 \cdot 10^{-2}$
4	$1.104 \cdot 10^{-1}$	$1.032 \cdot 10^{-1}$	$4.714 \cdot 10^{-1}$	$3.591 \cdot 10^{-3}$
6	$1.645 \cdot 10^{-2}$	$1.226 \cdot 10^{-2}$	$8.348 \cdot 10^{-2}$	$2.501 \cdot 10^{-4}$
8	$6.563 \cdot 10^{-4}$	$5.765 \cdot 10^{-4}$	$1.133 \cdot 10^{-3}$	$1.285 \cdot 10^{-5}$
10	$2.428 \cdot 10^{-5}$	$2.478 \cdot 10^{-5}$	$2.444 \cdot 10^{-5}$	$4.013 \cdot 10^{-7}$
12	$8.546 \cdot 10^{-7}$	$8.775 \cdot 10^{-7}$	$8.525 \cdot 10^{-7}$	$1.118 \cdot 10^{-8}$
14	$4.972 \cdot 10^{-8}$	$5.022 \cdot 10^{-8}$	$5.722 \cdot 10^{-8}$	$6.277 \cdot 10^{-10}$
16	$4.128 \cdot 10^{-9}$	$4.182 \cdot 10^{-9}$	$3.598 \cdot 10^{-9}$	$5.230 \cdot 10^{-11}$
18	$4.596 \cdot 10^{-10}$	$4.623 \cdot 10^{-10}$	$3.154 \cdot 10^{-10}$	$4.448 \cdot 10^{-12}$

Table 5: *The steady model problem for the Navier-Stokes equations on* $\Omega_{0.5}$*: Approximation errors for* $\Delta t = \frac{1}{10}$ *and* $\nu = 1$

As we observe from Table 5 the LSSCM leads to the high spectral accuracy for the velocity, the pressure and the divergence of the velocity field. Especially for larger polynomial degrees we observe the fast convergence of the proposed scheme.

5.2.2 Unsteady model problem

For the unsteady model problem we set $\gamma = 5$ in (20) – (22) on $\Omega_{0.5}$. For time integration we use the second order BDF scheme combined with the Adams-Bashforth scheme of order 2 for the convective term.
In Table 6 we show the results for $\nu = 1$. We set $t_{end} = 1$, since we have seen that the maximum error is obtained in $[0, 1]$.

Δt	E_{u_1}	ratio	E_{u_2}	ratio	E_p	ratio
$\frac{1}{10}$	$1.041 \cdot 10^{-2}$	—	$6.961 \cdot 10^{-3}$	—	$2.166 \cdot 10^{-1}$	—
$\frac{1}{20}$	$2.636 \cdot 10^{-3}$	3.949	$1.763 \cdot 10^{-3}$	3.948	$5.550 \cdot 10^{-2}$	3.903
$\frac{1}{40}$	$6.641 \cdot 10^{-4}$	3.969	$4.448 \cdot 10^{-4}$	3.964	$1.395 \cdot 10^{-2}$	3.978
$\frac{1}{80}$	$1.661 \cdot 10^{-4}$	3.998	$1.112 \cdot 10^{-4}$	4.000	$3.503 \cdot 10^{-3}$	3.982
$\frac{1}{160}$	$4.152 \cdot 10^{-5}$	4.000	$2.780 \cdot 10^{-5}$	4.000	$8.761 \cdot 10^{-4}$	3.998
$\frac{1}{320}$	$1.038 \cdot 10^{-5}$	4.000	$6.949 \cdot 10^{-6}$	4.001	$2.191 \cdot 10^{-4}$	3.999

Table 6: *The unsteady model problem for the Navier-Stokes equations on* $\Omega_{0.5}$*: Approximation errors for* $\nu = 1$*,* $N = 18$ *and* $t_{end} = 1$

From Table 6 we observe again, that the proposed scheme is of order 2, since the ratios of the errors converges to 4 when the time step size is halved.

Next, we consider the LSSCM for $\nu = \frac{1}{1000}$. The results are presented in Table 7.

Δt	E_{u_1}	ratio	E_{u_2}	ratio	E_p	ratio
$\frac{1}{1600}$	$9.746 \cdot 10^{-5}$	—	$5.951 \cdot 10^{-5}$	—	$8.435 \cdot 10^{-6}$	—
$\frac{1}{3200}$	$2.550 \cdot 10^{-5}$	3.822	$1.461 \cdot 10^{-5}$	4.073	$2.062 \cdot 10^{-6}$	4.091
$\frac{1}{6400}$	$6.594 \cdot 10^{-6}$	3.867	$3.608 \cdot 10^{-6}$	4.049	$5.114 \cdot 10^{-7}$	4.032
$\frac{1}{12800}$	$1.684 \cdot 10^{-6}$	3.916	$8.952 \cdot 10^{-7}$	4.030	$1.277 \cdot 10^{-7}$	4.005

Table 7: *The unsteady model problem for the Navier-Stokes equations on $\Omega_{0.5}$: Approximation errors for $\nu = \frac{1}{1000}$, $N = 18$ and $t_{end} = 1$*

Again, we observe that the LSSCM is second order, since the ratios of the errors converges to 4, see Table 7. It is clear that we have to use smaller time steps since the convective part becomes more dominant for decreasing ν. Our simulations have shown that using larger time step sizes Δt, the LSSCM becomes divergent.

5.2.3 Channel flow

Next, we consider the flow around the cylinder for the Navier-Stokes equations on $\Omega_{0,125}$. We simulate the channel flow for $\nu = 1$ and $\nu = \frac{1}{400}$. We choose $\nu = \frac{1}{400}$ as the smallest viscosity since then we reach a similar Reynolds number as in the DFG priority research program "Flow Simulation with High-Performance Computers II", see, e.g. [36]. For $\nu = 1$ we obtain a stationary flow. For $\nu = \frac{1}{400}$ we obtain a unsteady flow (oscillating) where the well-known "Von Karman Effect" occurs, i.e. vortices occur that move in the stream of the obstacle.

Again, we study the mass and momentum conservation of the proposed scheme and present the velocity and pressure profiles. To obtain the real conservation of mass and momentum we evaluate the numerical solution on CG nodes. Furthermore, we compute the loss of mass in the cross-section which is given by

$$\mathcal{M}_\psi := \int_{\gamma_1} \psi \, ds - \int_{\Gamma_2} \psi \, ds,$$

where γ_1 given in (25) and Γ_2 is defined as the union of the lines between '$(0, -0.75)$ and $(0, -0.125)$' and '$(0, 0.125)$ and $(0, 0.75)$', see Figure 12.
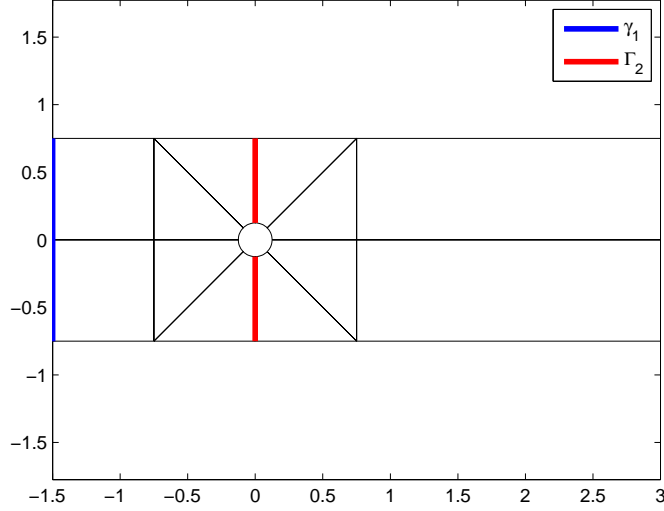
Figure 12: *Definition of γ_1 and Γ_2*

Here, we consider $\psi = u_1$, $\psi = u_2$ and $\psi = u_1 + u_2$ to see the influence of the different velocity components to the loss of mass within the cross-section. To verify the conservation of momentum, we consider the left hand side of (4) and define now

$$\mathcal{L}(U^{n+1}) := \frac{\frac{3}{2}\mathbf{u}^{n+1} - 2\mathbf{u}^n + \frac{1}{2}\mathbf{u}^{n-1}}{\Delta t} + 2\mathbf{C}^{n+1} - \mathbf{C}^{n+1} + \nu\nabla \times \omega^{n+1} + \nabla p^{n+1}.$$

That means, we use the computed solution (where we solve the system with the Δt-scaled momentum equations) and insert this one in the unscaled equations. Thus, we obtain the real conservation of momentum for the Navier-Stokes equations. For all computations in this section, we set $N = 16$.

5.2.4   Navier-Stokes equations with $\nu = 1$

First, we consider the Navier-Stokes equations with $\nu = 1$ and set $\Delta t = \frac{1}{10}$. In Figure 13 we show the loss of mass along the cross-section Γ_2 for the different ψ during time integration.
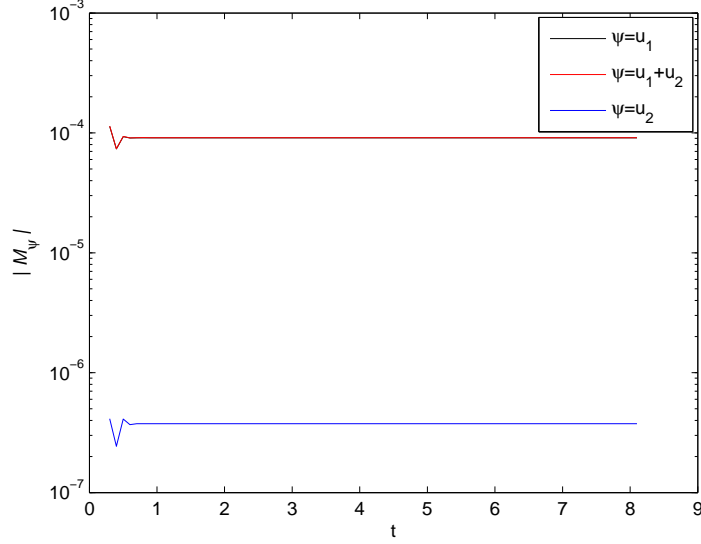
Figure 13: *Navier-Stokes flow past the cylinder on $\Omega_{0.125}$: Loss of mass along the cross-section Γ_2 during time integration for $\nu = 1$ and $\Delta t = \frac{1}{10}$, where $\psi = u_1$, $\psi = u_1 + u_2$ and $\psi = u_2$*

From Figure 13 we observe that for $\nu = 1$ the influence of velocity component u_2 to the loss of mass is negligible. Furthermore, our numerical solution shows a very good performance, since $|\mathcal{M}_{u_2}| \approx 10^{-7}$ and $|\mathcal{M}_{u_1}| \approx |\mathcal{M}_{u_1+u_2}| \approx 10^{-4}$. In Figure 14 we show $||\nabla \cdot \mathbf{u}||_{L^2}$ in the whole domain $\Omega_{0.125}$ during time integration. We observe that the divergence of the velocity field is about $7.5 \cdot 10^{-5}$. Thus, the proposed scheme is not only able to conserve mass within the cross-section but even in the whole domain.
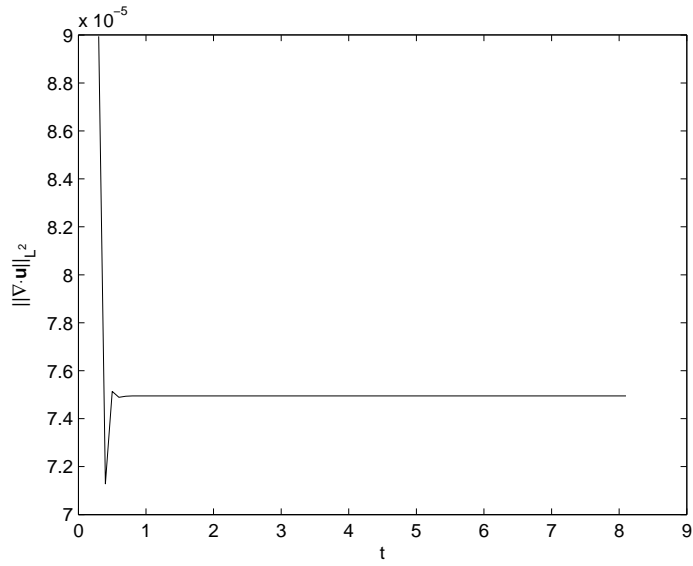
Figure 14: *Navier-Stokes flow past the cylinder on $\Omega_{0.125}$: $||\nabla \cdot \mathbf{u}||_{L^2}$ in the whole domain during time integration for $\nu = 1$ and $\Delta t = \frac{1}{10}$*

Figure 15 shows the momentum conservation during time integration.
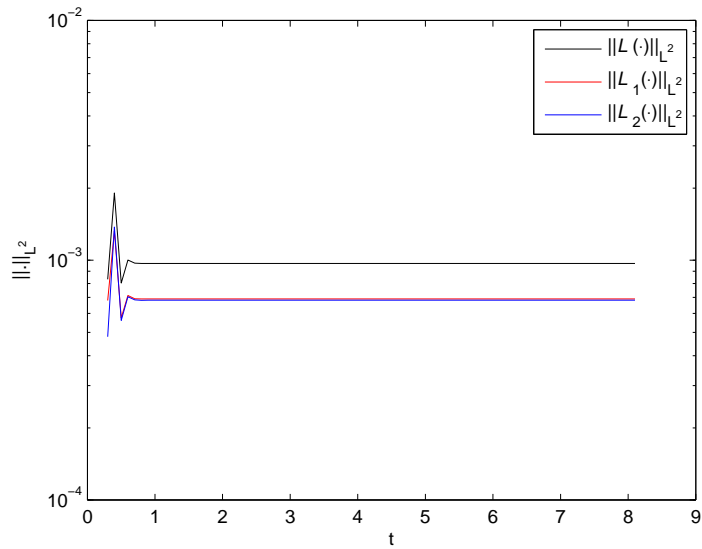
Figure 15: *Navier-Stokes flow past the cylinder on $\Omega_{0.125}$: Momentum conservation in the whole domain during time integration for $\nu = 1$ and $\Delta t = \frac{1}{10}$*

We show the conservation of both momentum components and of the whole momentum separately, i.e. $||\mathcal{L}_1(U)||_{L^2}$, $||\mathcal{L}_2(U)||_{L^2}$ and $||\mathcal{L}(U)||_{L^2}$. We observe that both of the components of the momentum are conserved approximately with the same accuracy ($\sim 10^{-4}$). The whole momentum $\mathcal{L}(U)$ is conserved up to $\sim 10^{-3}$. Again, we see that the proposed scheme leads to very good conservation of mass and momentum in the whole domain $\Omega_{0.125}$, see Figures 14 and 15.

In Figure 16 we show the profile of velocity component u_1 at different times during time integration. Since the problem with $\nu = 1$ leads to a stationary solution, we show only a few profiles. From the plots we observe that we obtain the same profiles during time integration, as expected.

$t = 1$

$t = 2$

$t = 4$

$t = 8$
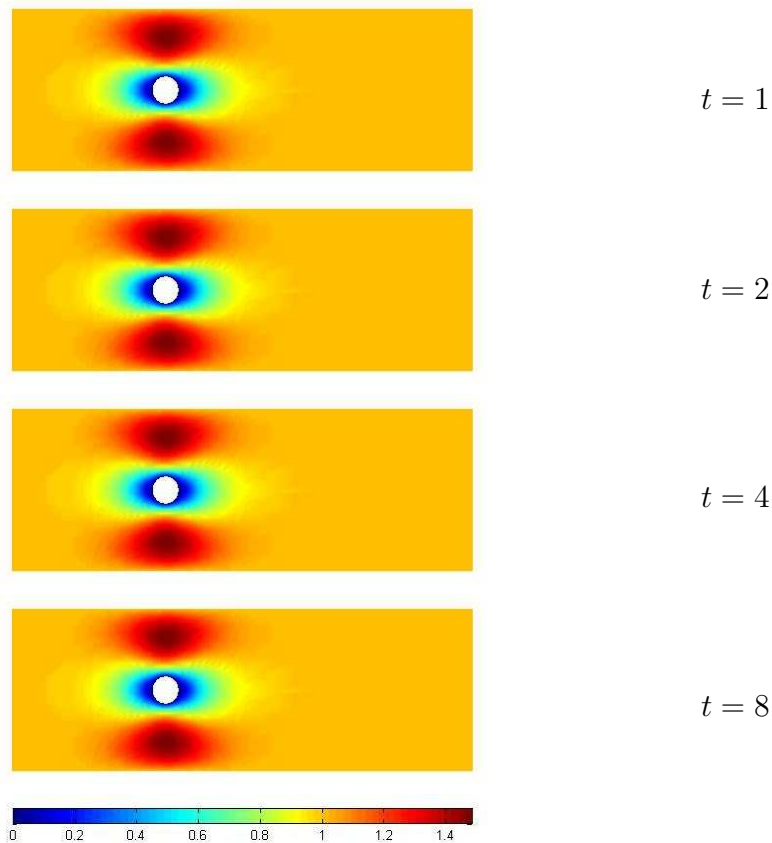
Figure 16: *Navier-Stokes flow past the cylinder on* $\Omega_{0.125}$*: Profile of* u_1 *at different times for* $\nu = 1$ *and* $\Delta t = \frac{1}{10}$

To show the convergence process of our computed solution we show in Figure

32

17 the temporal evolution of

$$\varepsilon := \frac{\max|\phi^{n+1} - \phi^n|}{\Delta t \cdot \max|\phi^{n+1}|},$$

where $\phi^T := [u_1, u_2]$ and the superscript n and $n+1$, respectively indicates to which time step the solution belongs. Again, $|\cdot|$ is the vector with the absolute value of its components. The oscillations in ε for $t \geq 3$ are caused by the influence of the round-off errors.
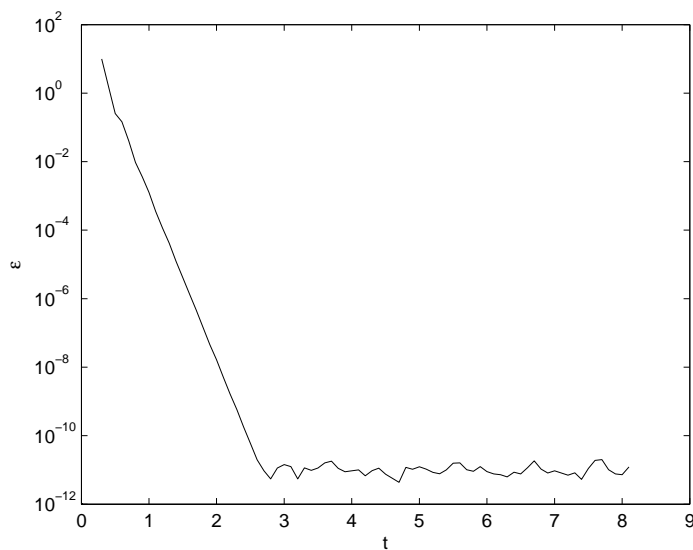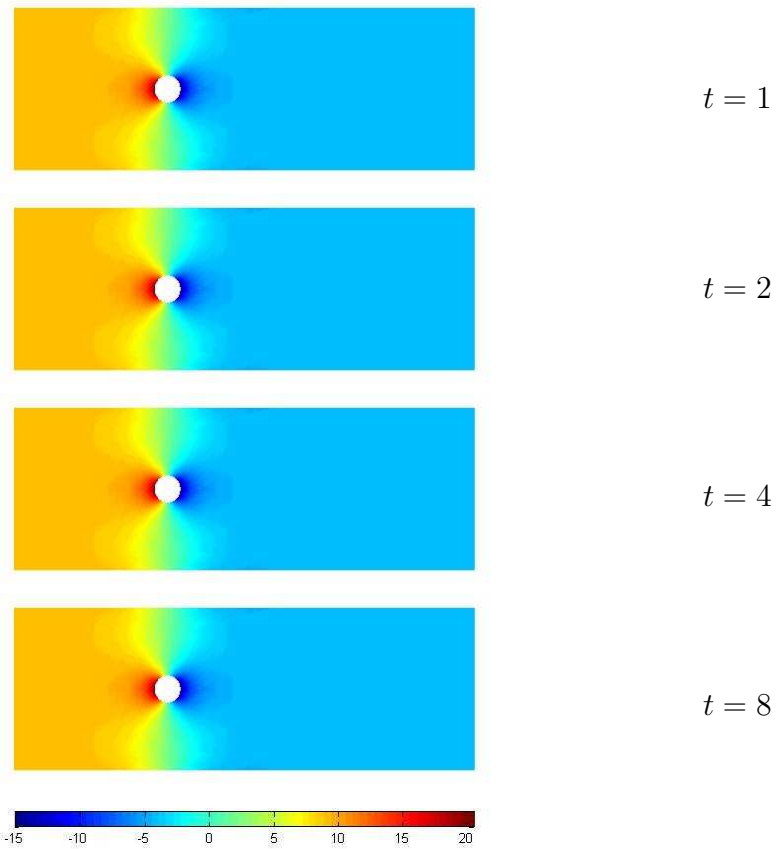

Figure 17: *Navier-Stokes flow past the cylinder on $\Omega_{0.125}$: ε during time integration for $\nu = 1$ and $\Delta t = \frac{1}{10}$*

From Figure 17 we observe again that the computed solution converges to a stationary solution.
In Figure 18 we show the profile of the pressure at different times during time integration.

Figure 18: *Navier-Stokes flow past the cylinder on*
$\Omega_{0.125}$: *Profile of p at different times for $\nu = 1$ and*
$\Delta t = \frac{1}{10}$

Again, we observe from Figure 18 the steady state.

5.2.5   Navier-Stokes equations with $\nu = \frac{1}{400}$

For the next simulations we set $\nu = \frac{1}{400}$ and use $\Delta t = \frac{1}{700}$. Our computations have shown that the LSSCM becomes divergent for larger time step sizes. In Figure 19 we show the loss of mass along the cross-section Γ_2 for the different ψ during time integration.
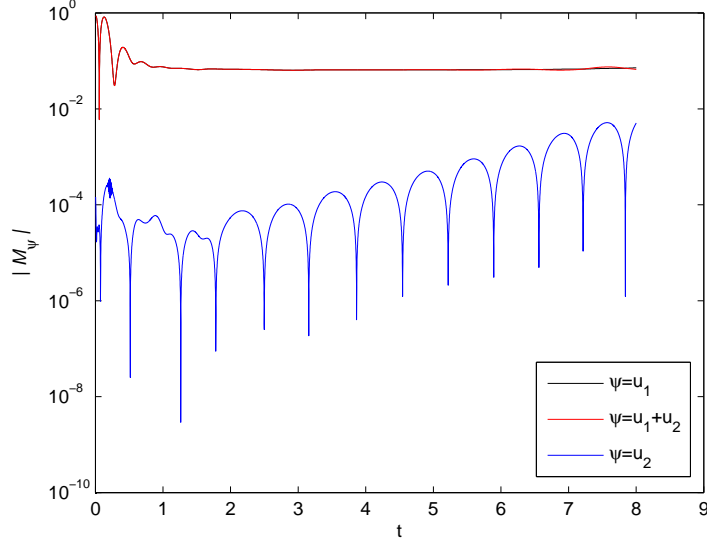
Figure 19: *Navier-Stokes flow past the cylinder on $\Omega_{0.125}$: Loss of mass along the cross-section Γ_2 for $\nu = \frac{1}{400}$ and $\Delta t = \frac{1}{700}$, where $\psi = u_1$, $\psi = u_2$ and $\psi = u_1 + u_2$*

We observe the typical oscillation of $|\mathcal{M}_{u_2}|$ during time integration. Since the collocation nodes are placed much closer in direction of the y-axis and because of the problem set-up it its clear that $|\mathcal{M}_{u_2}|$ is much closer to 0 than $|\mathcal{M}_{u_1}|$ and $|\mathcal{M}_{u_1+u_2}|$, respectively. Our computations have shown, that there is now blow-up of $|\mathcal{M}_\psi|$ for $\psi = u_2$ during time-integration. In Figure 20 we show the results for $\nu = \frac{1}{600}$, where it is obvious that there is now blow-up, even for larger Reynolds numbers.
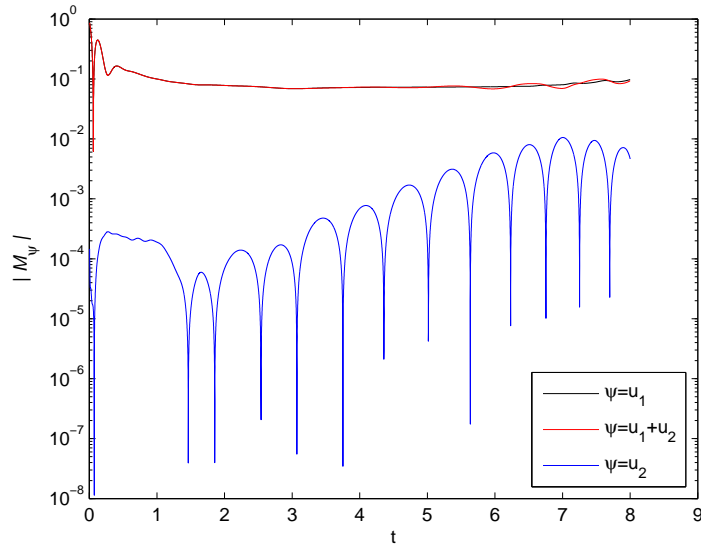
Figure 20: *Navier-Stokes flow past the cylinder on $\Omega_{0.125}$: Loss of mass along the cross-section Γ_2 for $\nu = \frac{1}{600}$ and $\Delta t = \frac{1}{1100}$, where $\psi = u_1$, $\psi = u_2$ and $\psi = u_1 + u_2$*

To show the slight difference between $|\mathcal{M}_{u_1}|$ and $|\mathcal{M}_{u_1+u_2}|$ for $\nu = \frac{1}{400}$ in Figure 19 we show in Figure 21 only these two values. Here, it becomes more clear that mass is conserved up to $\sim 10^{-2}$.
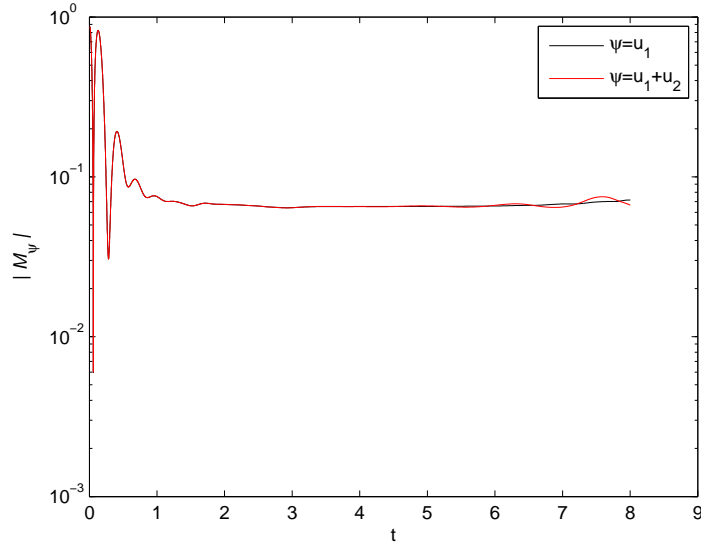
Figure 21: *Navier-Stokes flow past the cylinder on* $\Omega_{0.125}$*: Loss of mass along the cross-section* Γ_2 *for* $\nu = \frac{1}{400}$ *and* $\Delta t = \frac{1}{700}$*, where* $\psi = u_1$ *and* $\psi = u_1 + u_2$

Again, we observe from Figures 19 and 21 the oscillation at the beginning of time integration, caused by the start conditions for the second order BDF scheme and Adam-Bashforth scheme, respectively. The oscillation at the end of time integration is caused by the starting of the "Von Karman effect".

In Figure 22 we present $\|\nabla \cdot \mathbf{u}\|_{L^2}$ in the whole domain $\Omega_{0.125}$ during time integration. Again, we observe the good performance of the proposed scheme and the "Von Karman effect". Nevertheless, the LSSCM shows a very good conservation of mass in the whole domain for larger Reynolds numbers and smaller viscosities, respectively.
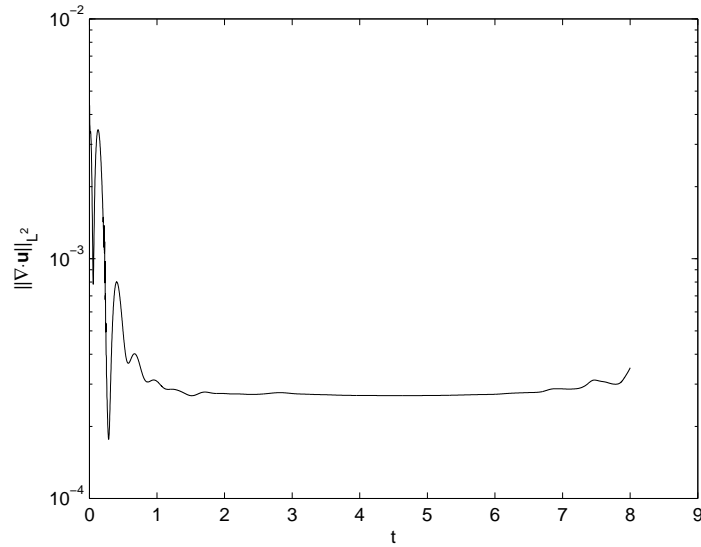
Figure 22: *Navier-Stokes flow past the cylinder on $\Omega_{0.125}$: $||\nabla \cdot \mathbf{u}||_{L^2}$ in the whole domain during time integration for $\nu = \frac{1}{400}$ and $\Delta t = \frac{1}{700}$*

In Figure 23 we present the conservation of momentum in the whole domain $\Omega_{0.125}$ during time integration. Again, we show $||\mathcal{L}_1(U)||_{L^2}$, $||\mathcal{L}_2(U)||_{L^2}$ and $||\mathcal{L}(U)||_{L^2}$ to see the influence of the different components.
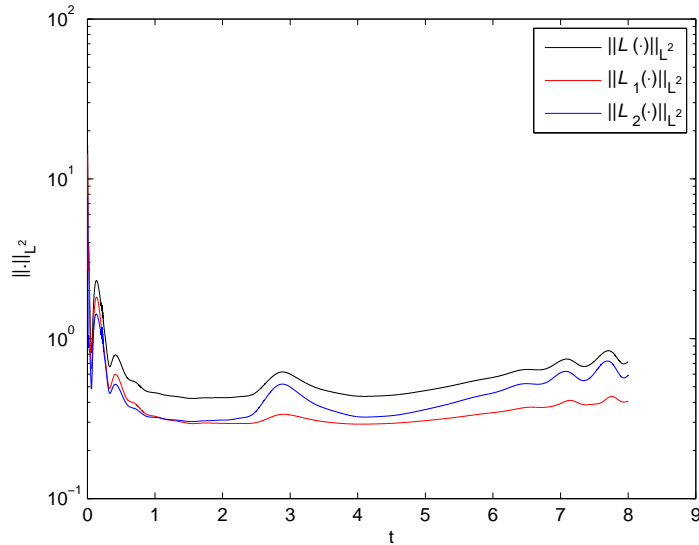
Figure 23: *Navier-Stokes flow past the cylinder on $\Omega_{0.125}$: Momentum conservation in the whole domain during time integration for $\nu = \frac{1}{400}$ and $\Delta t = \frac{1}{700}$*

All of the three values show an analog performance, as we see in Figure 23. The values increase slightly for $t > 4$ since the "Von Karman Effect" occurs (see, e.g. Figure 24) and therefore it is much harder to approximate the functions.

In Figure 24 we show the profile of velocity component u_1 at different times during time integration. From the different plots we observe the well-known periodic time-dependent profiles for the velocity.
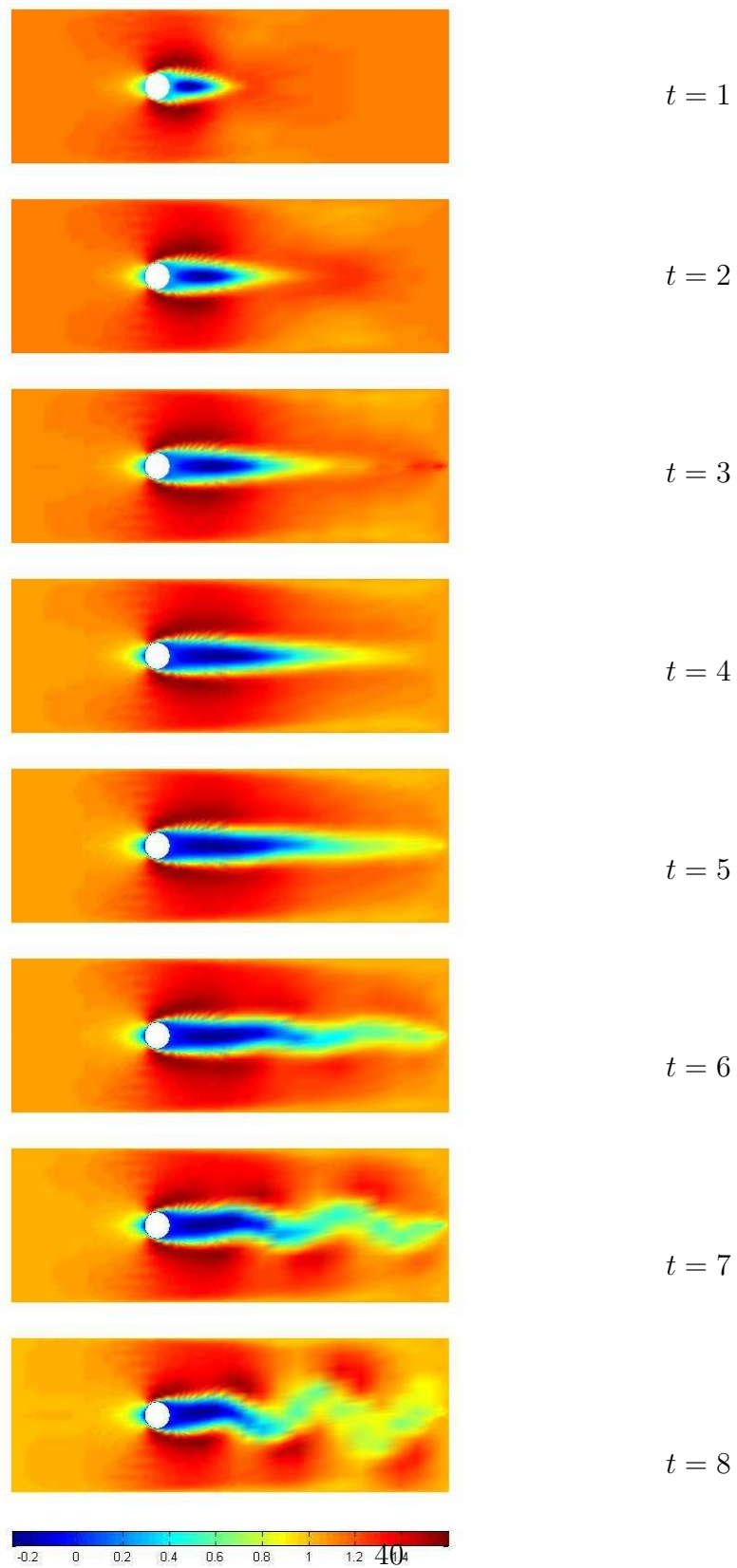
Figure 24: *Navier-Stokes flow past the cylinder on* $\Omega_{0.125}$*: Profile of* u_1 *at different times for* $\nu = \frac{1}{400}$ *and* $\Delta t = \frac{1}{700}$

From the results of our simulations (see Figures 19 - 24) for $\nu = \frac{1}{400}$ we observe that the LSSCM leads to good results concerning conservation of mass and momentum, respectively, and to the well-known performance for the channel flow problem. Furthermore, we observe the well-known profiles for the velocity, representing the good performance of the LSSCM.

6 Conclusion

We investigated mass and momentum conservation of the LSSCM for the time-dependent Stokes and for the Navier-Stokes equations. We used as test-problems internal flow problems, as in [3, 4] for LSFEM, in [33, 35] for LSSEM and as in [24] for LSSCM. For each of this methods only the stationary Stokes equations have been considered. Here, we continued the research in [24] for time-dependent problems. We observed that the LSSCM leads to very good results for this problems, too. The reasons that the LSSCM leads to good conservation can be found in:

1. We use only a few elements, each with a high polynomial degree.

2. We use a direct solver (QR decomposition) to solve the linear systems of equations. Avoiding solving by normal equations leads to algebraic systems with reduced condition numbers. Because of this we have less influence of round-off errors, see [15, 23, 24].

3. We did not set the pressure in one point, since we have shown in [15, 24] that the better way to avoid the natural mode is using the additional pressure condition in (7). Because of this we again reduced the condition numbers of the algebraic systems and this leads to a more stable scheme, see [15, 23–25].

4. We used the transfinite mapping of Gordon and Hall to discretize the internal flow problem. This leads to a high order approximation of the curved boundaries.

The main reason of the improved results can be found in using only a few elements with high-order approximation. The other improvements are only marginally, see [24]. All results are computed with the explicit scheme. We could also use the implicit scheme, but then the required CPU times are much higher, since the algebraic systems must be solved in each time step several times. Using the implicit scheme, we can use larger time step sizes compared to the explicit scheme. But since we here consider time-dependent problems we want to use small time steps.

References

[1] C. Bernardi C. Canuto, Y. Maday. *Generalized inf-sup condition for Chebyshev approximations to Navier-Stokes equations.* C.R. Acad. Sci. Paris, 303(serie I):971–974,1986. Springer, 1988.

[2] C. Canuto, M.Y.Hussaini, A. Quarteroni, T.A. Zang. *Spectral Methods in Fluid Dynamics.* Springer Series in Computational Physics. Springer, 1988.

[3] C. L. Chang, J. J. Nelson. *A mass conservative least-squares finite element method for the stokes problem.* Com. in Numer. Meth. in Eng., 11(12):965–970, 1995.

[4] C. L. Chang, J. J. Nelson. *Least-squares finite element method for the Stokes problem with zero residual of mass conservation.* SIAM J. Numer. Anal., 34(2):480–489, 1997.

[5] M. O. Deville, P. F. Fischer, E. H. Mund. *High-Order Methods for Incompressible Fluid Flow.* Cambridge Monographs on Applied and Computational Mathematics. Cambridge University Press, New York, 2002.

[6] A. Galvão, M. Gerritsma, B. De Maerschalck. *hp-adaptive least squares spectral element method for hyperbolic partial differential equations.* J. Comput. Appl. Math., 215(2):409–418, 2008.

[7] W. J. Gordon, C. A. Hall. *Construction of curvilinear co-ordinate systems and their applications to mesh generation.* Int. J. Numer. Meth. Eng., 7:461–477, 1973.

[8] W. J. Gordon, C. A. Hall. *Transfinite element methods: blending-function interpolation over arbitrary curved element domains.* Numer. Math., 21:109–129, 1973.

[9] D. Gottlieb, S. A. Orszag. *Numerical Analysis of Spectral Methods: Theory and Applications.* CBMS-NSF Regional Conference Series in Applied Mathematics, no.26. SIAM, 1977.

[10] W. Heinrichs. *Least-Squares Spectral Collocation for Discontinuous and Singular Perturbation Problems.* J. Comput. Appl. Math., 157(2):329–345, 2003.

[11] W. Heinrichs. *Spectral collocation schemes on the unit disc.* J. Comput. Phys., 199(1):66–86, 2004.

[12] W. Heinrichs. *Least-Squares Spectral Collocation for the Navier-Stokes Equations.* J. Sci. Comput., 21(1):81–90, 2004.

[13] W. Heinrichs. *Least-squares spectral collocation with the overlapping Schwarz method for the incompressible Navier-Stokes equations.* Numer. Algorithms, (43):61–73, 2006.

[14] W. Heinrichs. *An adaptive least-squares spectral collocation method with triangular elements for the incompressible Navier-Stokes equations.* J. Eng. Math., 56(3):337–350, 2006.

[15] W. Heinrichs and T. Kattelans. *A direct solver for the least-squares spectral collocation system on rectangular elements for the incompressible Navier-Stokes equations.* J. Comput. Phys., 227(9), 4776–4796 (2008)

[16] W. Hoitinga, R. de Groot, M. Kwakkel and M. Gerritsma. *Direct Minimization of the least-squares spectral element functional - Part I: Direct solver.* J. Comput. Phys., 227(4), 2411–2429 (2008)

[17] B.-N. Jiang and C. L. Chang. *Least-squares finite elements for the Stokes problem.* Comput. Methods Appl. Mech. Eng., 78(3):297–311, 1990.

[18] B.-N. Jiang and L. Povinelli. *Least-squares finite element method for fluid dynamics.* Comput. Methods Appl. Mech. Eng., 81(1):13–37, 1990.

[19] B.-N. Jiang. *A least-squares finite element method for incompressible Navier-Stokes problems.* Int. J. Numer. Methods Fluids, 14(7):843–859, 1992.

[20] B.-N. Jiang and V. Sonnad. *Least-squares solution of incompressible Navier-Stokes equations with the p-version of finite elements.* Comput. Mech., 15(2):129–136, 1994.

[21] B.-N. Jiang. *On the least-squares method.* Comput. Methods Appl. Mech. Eng., 152(1-2):239–257, 1998.

[22] T. Kattelans. *Spektrale Least-Squares Verfahren für inkompressible Navier-Stokes-Gleichungen.* Diploma thesis (in German), University of Duisburg-Essen, 2007.

[23] T. Kattelans and W. Heinrichs. *A least-squares spectral colloca-tion scheme with improved stability for the Stokes and the Navier-Stokes equations.* AIP Conference Proceedings of ICNAAM 2008, 1048: 307–310, 2008

[24] T. Kattelans and W. Heinrichs. *Conservation of mass and momen-tum of the least-squares spectral collocation scheme for the Stokes problem.* J. Comput. Phys., 228(13), 4649–4664 (2009)

[25] T. Kattelans. *The least-squares spectral collocation method for incompressible flows.* Dissertation University of Duisburg-Essen. Verlag Dr. Köster, Berlin (2009)

[26] S. A. Orszag. *Spectral methods for problems in complex geometries.* J. Comput. Phys., 37:70–92, 1980.

[27] R. Peyret. *Spectral Methods for Incompressible Viscous Flow.* Springer, 2002.

[28] J. P. Pontaza and J. N. Reddy. *Spectral/hp least-squares finite element formulation for the Navier-Stokes equations.* J. Comput. Phys., 190(2):523–549, 2003.

[29] J. P. Pontaza and J. N. Reddy. *Space-time coupled spectral/hp least-squares finite element formulation for the incompressible Navier-Stokes equations.* J. Comput. Phys., 197(2):418–459, 2004.

[30] J. P. Pontaza and J. N. Reddy. *Least-squares finite element for-mulations for viscous incompressible and compressible fluid flows.* Comput. Methods Appl. Mech. Eng., 195(19-22):2454–2494, 2006.

[31] M. M. J. Proot and M. I. Gerritsma. *A Least-Squares Spectral Element Formulation for the Stokes Problem.* J. Sci. Comput., 17(1-4):285–296, 2002.

[32] M. M. J. Proot and M. I. Gerritsma. *Least-Squares Spectral Elements Applied to the Stokes Problem.* J. Comput. Phys., 181(2):454–477, 2002.

[33] M. M. J. Proot. *The Least-Squares Spectral Element Method. Theory, Implementation and Application to Incompressible Flows.* Ph.D thesis, Delft University of Technology, 2003.

[34] M. M. J. Proot and M. I. Gerritsma. *Application of the least-squares spectral element method using Chebyshev polynomials to solve the incompressible Navier-Stokes equations.* Numer. Algorithms, 38:155–172, 2005.

[35] M. M. J. Proot and M. I. Gerritsma. *Mass- and Momentum Conservation of the Least-Squares Spectral Element Method for the Stokes Problem.* J. Sci. Comput., 27(1-3):389–401, 2006.

[36] M. Schäfer and S. Turek: *Benchmark computations of laminar flow around a cylinder.* in E. H. Hirschel (editor), *Flow Simulations with High-Performance Computers II*, Vol. 52, Notes on Numerical Fluid Mechanics, 547–566, Vieweg 1996.

[37] L. N. Trefethen. *Is Gauss Quadrature Better than Clenshaw–Curtis?* SIAM Review, 50(1): 67-87 (2008).